We thank the reviewers for their many very helpful comments and insightful suggestions. The plots and discussions were improved and many descriptions are now more precise.

We do not repeat minor technical suggestions, e.g., for wording, unless we did *not* apply them straightforwardly. Attached in the end is the revised paper with additions/deletions marked in red and blue colours.

1   Reply to Referee #1

1.1   Major Comments

1. *I have only one main concern that, probably, can be solved by including a mini-mal discussion. To generate IRLS synthetic measurements, the authors assume a FTS spectral resolution $1/(2\,MOPD)=1.25\,cm^{-1}$, that is more than a factor of 6 worse than the required value for this instrument to study atmospheric chemistry. Such a strong reduction of the spectral resolution makes it possible to implement a very fine spatial sampling step, as the time interval required for the individual measurements is reduced accordingly. This instrument setup is very favourable to study clouds which generally have broad spectral features and are scattered in space. On the other hand, most likely, measurements made in this configuration will not allow retrieving gas profiles with sufficient accuracy. Therefore, I feel that this instrument operating mode in practice could be commanded only rarely. The mea-surements the authors use for their 2D tomographic retrieval of the cloud extinction seem limited to the spectral radiances integrated in two narrow spectral intervals. Probably, these measurements could be acquired with an instrument much cheaper than the considered IRLS interferometer. Maybe, a 2 channels calibrated imager pointing at the limb could be sufficient?*

   In conclusion, I recommend to publish this paper in AMT, however the authors should at least include a minimal discussion regarding the above issue, and clarify / correct the text according to the specific and minor comments included below.

   Lines 85–88: see my main comment above. The configuration you assume (spectral sampling $= 1.25\,cm^{-1}$ and fine spatial coverage) is certainly optimal to investigate cloud propertied which generally have broad spectral features. However, the IRLS mission had additional science objectives (gases retrieval) which, probably, cannot be met if such a low spectral resolution is commanded. So, although feasible, I imagine this operation mode can be used only for very limited time periods. Could-you please comment / address this point?

   Lines 178–180: same comment as above (regarding lines 85–88). Please note that for CI analyses, a much cheaper instrument such as a two channels calibrated imager could be sufficient. If the IRLS instrument will be implemented on a real satellite, you may hardly ask to operate it with so low spectral resolution and fine spatial sampling just to perform the CI analysis, if the spectral resolution is degraded, a lot of information on gases spectral lines is lost.

   The instrument was designed with two major operating modes in mind, one exploring the atmospheric dynamics (major circulation systems, gravity waves, UTLS exchange by means of water vapour, CFCs and ozone) modelled more after the CRISTA satellite and one ded-icated to examining the chemical composition of the atmosphere modelled more after the (nominal operating mode of the) MIPAS-ENVISAT instrument. Both operating modes were always seen as equally important and neither was a "special, seldom to be used" mode. The exact way to split the observation time was not finally settled, but the following was noted in the report for assessment: *The typical operation time of one mode is between one orbit and one week or even more. The baseline is for observing times to be comparable in the two modes..* This equal split should give a sufficient amount of observations for proper statistical

evaluation of data from both modes (e.g., gravity wave occurrence and chemical composition). The quantities of temperature, water vapour, ozone, and CFCs would be continuously available during both modes (albeit with maybe different spatial characteristics).

Please note also that many more trace gases were derived from measurements of the CRISTA spectrometer, which also had a spectral resolution much coarser than the IRLS CM mode. While this was not investigated in detail, it is plausible that more than the above listed trace gases could be derived from DM mode measurements (although not the full range of those available from scientific processors evaluating MIPAS-ENVISAT measurements, obviously).

For an instrument solely dedicated to gravity waves (or cloud shape retrieval for that matter) a simpler radiometer might be sufficient, even though it would be certainly less accurate (the resolved spectrum allows to better remove emissions of background gases and better overall calibration). However, the scientific requirements for the IRLS to derive water vapour and ozone highly spatially resolved in the UTLS makes a FTS already much more attractive, the possibilities of exploiting the remainder of the spectrum for other objectives aside. A HIRDLS-like successor instrument could likely fulfill most of the requirements of the IRLS dynamics mode, though.

We added to the IRLS instrument description: *This corresponds to the 'dynamics mode', which was envisioned to be used for about half of the instrument measurement time; its primary purpose was a high spatial resolution to reveal processes associated with mixing and convective outflow in the UTLS, as well as three-dimensionally resolving gravity waves to determine momentum fluxes driving global circulation systems (ESA, 2012).*

1.2 Specific Comments

1. *Lines 34–36: please note that the tomographic 2D retrieval for satellite limb measurements dates back to Carlotti et al. 2001 (I suggest to cite this paper also here, just before Steck et al. 2005). Due to technology limitations, MIPAS/ENVISAT was not an imaging interferometer. This implied that the sampling strategy had to give priority to vertical coverage and vertical sampling step rather than to the horizontal sampling. Despite of that, MIPAS limb measurements had overlapping line-of-sights, especially in the measurements acquired after 2004. Due to this characteristics of MIPAS measurements, a database of Level 2 products obtained with the 2D tomographic approach was established: see Carlotti et al. 2006 and Dinelli et al. 2010. Even if now you are getting much better results due to the improved characteristics of the planned (IRLS) and available (GLORIA) measurements, I suggest to give proper recognition also to the above mentioned work and to correct the statement at line 36, which is not true (e.g. the special MIPAS observation mode S6 was specifically designed for tomographic retrievals, see http://eodg.atm.ox.ac.uk/MIPAS/frmodes.html).*

We will correct the text and also cite the Carlotti paper, which predates the given cites by quite a bit.

The L2 products of MIPAS, as those of other conventional limb sounders, improve greatly by using tomographic measurement techniques. However, the main advantage for a tomographic retrieval of MIPAS data is not an increased spatial resolution, but the increased reliability against gradients in trace gases and temperature along the line-of-sight (a *very* important feature for limb sounders, but not the subject of this particular study), not the spatial horizontal resolution. And while lines-of-sight overlap, they do so only in "higher" layers, not close to the tangent point layer. The special tomographic measurement mode of MIPAS, with a horizontal spacing of 180 km, would indeed increase the spatial resolution compared to the figures of 200 to 500 km for the horizontal resolution of the nominal operating mode given by von Clarmann et al. (2009), and it served well as a proof of concept for this capability. We adopted the text:

,,While tomographic retrievals have become state of the art for limb sounders in general (e.g. Livesey and Read, 2000; Carlotti et al., 2001; Steck et al., 2005; Livesey et al., 2006; Christensen et al., 2015), in-orbit instruments do not oversample extensively; e.g., the MIPAS instrument on ENVISAT (Fischer et al., 2008) was operated to have in nominal measurement modes non-overlapping lines-of-sight in the tangent layer. Tomography was, due to instrument limitations, mostly performed to increase the retrieval accuracy in the presence of gradients in retrieved quantities along the line-of-sight."

2. *Line 75 "to point its detector...": I guess it is the "line of sight" which is adjusted, not the detector itself.*

GLORIA does not use mirrors for its pointing, but actually moves the whole spectrometer, including the detector, in a 3-D gimbal mount. To avoid confusion, we changed the text to *,,to point the instrument".*

3. *Line 86, "15 horizontal measurement tracks covering 7°": do you mean across track measurements with line-of-sight spanning an angle of 7 degrees in azimuth?*

We adopted the text to state *,,±3.5°".*

4. *Line 143: I believe CI is the ratio between the integrated spectral radiance in two different spectral intervals, not the "ratio between spectral regions" as mentioned here.*

The suggestion is indeed more precise. We updated the definition to *,,The CI is defined as the ratio between the radiance averaged over a spectral region with a strong emission feature, such as the CO_2 Q-branch at 12.6 μm, and the radiance averaged over an atmospheric window, such as the one located at 12 μm. "*

5. *Line 213: the computing power of current PCs varies by orders of magnitude, please give the main technical details of the platform in which you tested the algorithm.*

The system was a *,,AMD EPYC 7351P 16-Core Processor operating at 2.9 GHz",* which was amended in the text.

6. *Line 252: do you also add pseudo – random noise to the synthetic measurements? Does the measurement noise have an impact on the results presented?*

We included consistently 0.8 nW/(cm^{2}srcm^{-1}) corresponding to the envisioned noise level of the IRLS instrument for microwindows of the given width. But we found this noise to be insignificant for the task at hand. We did not use a different noise specification for MIPAS to stay consistent, especially as no effect was noticeable. The focus is to compare the relative spatial detection capabilities and not the detection thresholds.

We added *,,To focus on the relative capabilities of the algorithms, we added Gaussian noise to simulated MIPAS or IRLS measurements with a standard deviation of 0.8 nW/(cm^{2}srcm^{-1})."*

7. *Line 228: why do you retrieve the temperature profile? The ECMWF estimate is not sufficiently accurate for your purposes? For each sweep of the limb scan, the measurements included in the inversion seem limited to the two values of the integrated radiance in the two spectral intervals (centered at 796.25 cm^{-1} and 835.00 cm^{-1}). How the number of observations compares to the number of retrieved parameters? My concern is that temperature and extinction could be very correlated in your inversion, thus in real retrievals, forward model errors (like interference errors or model errors due to neglecting scattering) could impact strongly on the retrieved extinction, that is the target of interest to you.*

We assume that ECMWF temperature is typically known well enough. Except for extreme circumstances, such a heavy small-scale gravity wave activity, we seldom found ECMWF

off by more than 3 K in recent aircraft campaigns. However, with 2-D tomography one is typically able to derive temperature without too much hassle such that one does not need to rely on assumptions (always preferable). When not retrieving temperature, we'd have needed to model the assumed discrepancies of ECMWF and estimate the effect on extinction, strictly because of the correlation between them. We believed the setup to be more realistic and difficult by including the temperature in the retrieval study.

For the 3-D GLORIA example, we assumed ECMWF to be sufficiently correct to drastically simplify the very costly, and also more unstable, 3-D retrieval.

For the satellite extinction retrievals, there are typically twice as many unknowns as measurements. This is largely due to atmospheric state parameters in boundary regions (above, below, left, right) and some minor over-sampling.

We also believe the listed error sources to impact the derived extinction value. Especially scattering can cause an error in the double-digit percentage range. It causes, typically, an overestimate in the derived extinction, as warmer radiances from lower layers or the ground are scattered into the line-of-sight. As such, scattering improves the cloud detection capability. Please note that scattering also impacts cloud detection by colour ratios.

An error in temperature should have, generally, also a small effect, percentage wise. The signal generated by clouds is typically so large that even large errors will not cause us to "miss" the cloud.

Evaluating the derived extinction quantitatively to derive cloud parameters such as ice water path, etc., would require a more careful approach.

8. *Lines 238 and ff: please explain the meaning of all the symbols appearing in Eq. 1. The Levenberg–Marquardt damping, the Jacobian F', and the iteration index i are not defined.*

We amended the section to include the missing information.

9. *Line 238: you assume 0.1% error on the integrated radiances. Is this error figure compliant with MIPAS / IRLS NESR specifications?*

No, it isn't. The noise added to the measurements was defined according to the IRLS specification (see above), but it is insignificant here compared to the relative error caused due to the use of different grids for generating the synthetic measurements and performing the retrieval. We added: *,,The matrix $\mathbf{S}_\epsilon$ is set up assuming a 0.1 % error in radiance, which has been chosen to allow for differences caused by the use of different grids for generating the synthetic measurements and the retrieval itself."*

10. *Lines 242 and 243: regarding the constraint applied to extinction, it is not clear whether you constrain only the first derivative or also the actual retrieved values (usually, this would not be called regularization). Which first derivative do you constrain? The horizontals, the vertical, or all?*

We rephrased more specifically: *For extinction, the first derivatives in both spatial directions are constrained using the same correlation lengths in addition to imposing a weak constraint of the absolute extinction values towards the zero profile.*

11. *Line 249: presumably here you refer to the amount of RAM required. I would use the more common unit of Megabyte (MB) instead of the Mebibyte (MiB). By the way, the difference between the two is only 4.9%, thus not really relevant.*

We changed the unit, which, due to rounding, does not matter, indeed.

12. *Lines 256–257: not obvious to me, I recommend to include at least a "minimal" explanation.*

We added a reference to the figure and an explanation as *,,The 'pixels' corresponding to MIPAS measurements in Fig. 2b are very coarse compared to the fine structure of the clouds*

4

contained in the CALIOP data due to the much sparser horizontal sampling density of the MIPAS instrument."

13. *Line 273: did-you mean "a coarser horizontal retrieval grid"?*

Yes. We changed the text accordingly.

14. *Figures 2 to 6: could you specify somewhere, where is the satellite instrument located in these figures? I guess the satellite is on the left, given the difficulty to detect exactly the Cloud Top on the right side of the more opaque clouds.*

The satellite is not located at one position only, as this is a tomographic measurement, i.e., it combines the measurements of the satellite from multiple positions. We added the sentence *,,The satellite looks northwards in these simulations."* to the captions of these figures.

15. *Figures 2 to 7: the top title is not very informative for the readers, it could be removed.*

We complied and added the information into the caption, where we found this necessary.

16. *Lines 338–339: in panel (e) of Figure 9, I would have expected to see the retrieved extinctions, however the text is not very explicit on this point. Moreover, the caption of Figure 9 states that panel (e) shows the extinction values "used for generating the simulated measurements". This is confusing, could-you please clarify what you are really showing?*

To be more consistent with the previous figures, we moved the row e) to the top. This is indeed the extinction used to perform the simulations. As mentioned in the main text, we only employed the CI based methods on the CLaMS 3-D data. We also changed the cloud-shape result to the same white-blue colour scale used in the previous plots.

Lines 341–347: this is strange again. From the left plot of panel (d) on Fig. 9, I see that the CI determined on the basis of the convex hull, results with cloudy pixels at 5 km at latitudes of 45–50 degrees North. However, looking at panel (b) of Fig. 10, it does not seem that the cloud system extends down to 5 km. Again, here I don't understand why in Fig. 10b you don't plot the 0.001 km^{-1} contour surface of the retrieved extinction, which should give the best performance. Did I misunderstand something? Please clarify.

This confusion is the result of the unfortunate placement of the "true extinction" in the preceding plot, which was corrected. This 3-D CLaMS section focuses on the convex hull algorithm for cloud shape retrievals and not the extinction retrieval. The focus of this section is less to compare the different methods, but to demonstrate the 3-D capabilities. We also assume that a tomographic extinction retrieval (2-D or even 3-D) would deliver slightly superior results as before, but did not actually set it up.

17. *Lines 359–362: why do you change the retrieval approach in the case of GLO-RIA measurements? Specifically, why the ECMWF temperature is considered sufficiently accurate for this case and not enough accurate in the test simulations presented ear- lier? I agree that if you do not retrieve temperature, the microwindow centered about 796.25 cm^{-1} is no longer required, however, you also change the second microwindow that in earlier tests was centered about 835.00 cm^{-1}. Why? Please justify. Please, justify also the choice of ignoring gases concentrations in this retrieval.*

Due to historical different use of cloud index spectral regions between satellite and airborne instruments, there were some inconsistencies between the satellite simulations and the GLO-RIA retrieval. We consolidated the microwindow region employed for GLORIA data to 831.2 to 835.0 (still slightly different due to the given spectral sampling of 0.2 wavenumbers in the

level 1 data, but as close as feasible). This microwindow is now also consistently used for the retrieval and all depictions of GLORIA IR images and brightness temperatures. The retrieval results changed only insignificantly. We explained the reasoning for discarding the temperature retrieval and CO2-Q-branch window better in the main text: *,,We used all images taken between 11:10 UTC and 12:35 UTC in the reconstruction. The 3-D retrieval is computationally significantly more expensive compared to the 2-D retrievals as the number of unknowns is much higher and the involved algorithms scale with a power of given unknowns. The atmospheric volume is also much less constrained by the measurements as the number of unknowns vastly outnumbers the measurements and the distribution of information is far from homogeneous. We found that deriving temperature and extinction similar to the 2-D setup works well within the volume covered by tangent points, but quickly deteriorates outside. Thus, we neglect the temperature retrieval here, as this improved the retrieval on three fronts. First, this allows discarding of the 792 cm^{-1} window and to not take any trace gas emissions into account in the forward modelling, drastically improving the forward model speed by orders of magnitude. Second, it halved the number of unknowns, thereby increasing convergence speed of iterative solvers by a factor of roughly four and decreasing memory consumption by half. Third, this also stabilized the extinction retrieval such that the extinction values outside the core volume are less affected by retrieval artifacts. The employed single microwindow averaged all spectral samples between 831.2 cm^{-1} and 835.0 cm^{-1} (GLORIA operated in a mode that allows for a spectral sampling of 0.2 cm^{-1} during this portion of the flight)."*

18.   *Lines 364–365: It seems that two cameras were operating together with GLORIA in this flight. Please introduce earlier all the instruments used and define also the main features of the cameras, e.g. which is their spectral band-pass?*

Lines 365–368: not clear at all. Maybe it will be more clear when the operation mode of the two cameras will be better explained.

There are just two 'cameras' contained in GLORIA: the main camera is the IR spectrometer, which has been described in detail, while additionally a "standard" camera in the visible range of the spectrum has been mounted; this secondary camera has several technical issues that make it difficult to use the data scientifically except for getting a better overview of an imaged situation. Information about the passband characteristics of the optics or the sensitivity of the RGB detector pixels are not available and there were so far also no calibration efforts. It has been used so far to get an overview of the imaged situation in a larger context due to the wider FOV.

We added *,,In addition to the IR instrument, there is also a standard camera with three channels (red/green/blue) operating in the visible range that observes a much wider field-of-view"* to the instrument description.

We also updated the caption of the image to *,,A superposition of a visible and infrared image taken at 11:50:31 UTC showing a cirrus cloud located at 10.5 km. The visible image has a much wider field-of-view than the infrared one. The infrared image has been extracted from the spectrally resolved GLORIA measurements and shows the averaged radiance over the spectral range from 831.2 cm^{-1} to 835.0 cm^{-1}; it has also been shifted to the right for better comparability and the radiance is depicted in a logarithmic scale with arbitrary units;"* to clarify that the IR image has not been taken by a third instrument, but has been taken by GLORIA (it is an imager after all).

19.   *Line 374: the inversion problem is said to be "ill-conditioned" (and this is especially true because relatively few measurements were used in the inversion, as compared to the amount of retrieval parameters).*

The inverse problem is under-determined and has thus a non-trivial null-space. Thus, it is certainly ill-conditioned. It is ill-posed as well. The approximation of the original problem by the regularized problem takes care of both issues.

We expanded the text ,,*This number is significantly larger than the number of measurements, making this a drastically under-determined problem.*

The inverse problem, i.e., identifying an atmospheric state fitting to the measurements, is an ill-posed problem. To solve it, we approximate it by a well-posed, regularized formulation. To regularize the problem, we employ constraints of zero-th and first order. "

20. *Line 379: please specify how you define the "well resolved region". How many degrees of freedom (DOF) do you have, for each retrieval grid point, in the well resolved region?*

    Lines 395–400: I think a Figure with some maps reporting the number of DOFs per retrieval grid point at some fixed altitudes would be more illustrative and clear than this qualitative explanation.

Such a plot would be obviously very useful, but is too expensive to compute for the given, highly resolved setup. For other setups, we found the region withing the volume covered by tangent points to have a consistent, good resolution, while the shape of the AVK outside becomes quickly very irregular making already the definition of a FWHM resolution difficult (Ungermann et al., 2011; Ungermann, 2011; Krisch et al., 2018).

Computing a row of the AVK is only slightly one order of magnitude less expensive as the full retrieval and any cross-section has ten-thousands of points. But we computed the degrees of freedom for selected representative points inside and outside the well-resolved volume. Inside the well-resolved volume typical values are in the order of 1/20, i.e. about 20 samples share one piece of information. This value is to be expected with the oversampling of the atmosphere. Outside, it drops to about an order of magnitude less.

Accessing the trace of the AVK is sadly infeasible as well; at least we have not found a way to access it for retrievals of this size, yet.

A full diagnostic is only feasible for retrievals with a few ten thousands of unknowns due to the computational effort and numerical instability. 2-D satellite retrievals are at the border of this figure, but can be typically set up in a way to be smaller.

We added the DOF figure as ,,*Within the well-resolved volume the analysis shows an information content of about 0.05, i.e. 20 samples share about one degree of freedom; outside it drops to an order of magnitude less, but numerical instabilities of the involved equation systems makes the latter difficult to compute precisely.*". Resolution as FWHM in km was already specified before.

21. *Figure 11: please add labels in the horizontal and vertical axes. In the figure caption, I guess you meant "visible" in place of "visual". The top title does not provide useful information to the reader.*

We added the labels, the title, and replaced visual with visible.

22. *Line 383: which instrument measured the brightness temperatures reported in Fig. 12? GLORIA? To which wavenumber or spectral band do the reported brightness temperatures refer?*

The brightness temperature was measured by the GLORIA IR spectrometer. The spectral range was added as: ,,*Brightness temperature of GLORIA measurements averaged over the wavenumber range from $831.2 \, \text{cm}^{-1}$ to $835 \, \text{cm}^{-1}$ (the same that is used as in the tomographic retrieval) over time sorted according to azimuth angle in relation to aircraft heading.*"

23. *Lines 384–393: the retrieval or inversion of measurements is the "rigorous" approach while, I guess, this is a qualitative interpretation of auxiliary / additional measurements that were not adequately introduced.*

This is a qualitative interpretation of the actual measurements being used in the retrieval. The brightness temperatures depicted were derived from the GLORIA measurements used

in the retrieval (which has been made clearer in the caption). Only the retrieval is able to do a quantitative and optimal interpretation (rigorous approach), but an intuitive approach also works up to a certain degree and is useful to determine expectations with respect to retrieval outcome and help in interpretation thereof.

We clarified this as *,,Figure 12 shows the measured brightness temperatures of the averaged microwindow used in the retrieval taken at different azimuth angles. Just these three given angles give already some insight into the real cloud structure (while the retrieval has also access to the full set of angles)."*

24. *Line 442: extinction is in km^{-1} . From Fig. 13, the extinction of cloud B seems of the order of 0.01 km^{-1} . Please explain how you infer the extinction of 0.1 km^{-1}*

There were a couple of issues with the numbers used in this estimate.

Looking at the underlying data, the brightness temperature surrounding the observed cloud towards East is 274.3±0.5K. The brightness temperature of the cloud in the region imaged by GLORIA is 272.7±0.5K. The cloud itself is slightly thicker than 1 km, between 1.25 and 1.5 km. The extinction varies also over it with values of up to 0.017 km^{-1}. (and here, a zero was indeed missing!). We adopted the colour scale of the GLORIA result plot to make the higher values more visible.

These values can be used for a rough estimate that results in a smaller transmissivity of a vertical ray through the cloud of $\exp(- \approx 1.5 \cdot \approx 0.014) \approx 0.98$. Applying this transmittance to the ground level brightness temperature (274.3 K) causes a drop in brightness temperature by about 1.3 K to 273.0 K neglecting emission/scattering by the (comparatively cold) cloud itself.

We modified the paragraph to *This cloud is ≈ 1.5 km thick with an extinction of ≈ 0.014 km^{-1} and hence, should reduce the measured nadir brightness temperature by ≈ 1.3 K, which is roughly consistent with the difference of 1.5 K observed by SEVIRI between the cloud and surrounding air.*

25. *Lines 236–237: all symbols of the equation are either vectors or matrices, therefore I would not use italic fonts. Unlike the others, the last "F" is italic. Line 233: for "F" I would use bold, roman fonts everywhere.*

We follow the guideline of AMT to use bold letters for matrices and bold italics for vectors. We interpret this to be applicable to matrix- and vector-*valued* functions as well. As such $\boldsymbol{F}$ is formatted with 'vec' while $\mathbf{F}'$ is formatted with 'mat'.

2 Reply to Referee #2

2.1 Comments

1. *L34-L37: Some earlier work on 2D retrievals is omitted in this discussion e.g. as cited in Ungermann (2013) . . . see p16 . . . "This is in principal similar to the concept of tomographic 2-D retrievals of satellite limb sounder data, which were first produced by Carlotti et al. (2001) and Steck et al. (2005) for the Michelson Interferometer for Passive Atmospheric Sounding (MIPAS) and by Livesey and Read (2000) for the Microwave Limb Sounder."*

   - *Massimo Carlotti, Bianca Maria Dinelli, Piera Raspollini, and Marco Ridolfi, "Geo-fit approach to the analysis of limb-scanning satellite measurements," Appl. Opt. 40, 1872-1885 (2001)*
   - *Nathaniel J. Livesey and William G. Read, "Direct Retrieval of Line-of-Sight Atmo- spheric Structure from Limb Sounding Observations", GEOPHYSICAL RESEARCH LETTERS, VOL. 27, NO. 6, PAGES 891-894, MARCH 15, 2000*

The list was by no means intended to be comprehensive. We agree, that the listed papers predate the given references by a couple of years and should thus be added.

2.   *L61-L62: Wasn't most of the MIPAS mission carried out with the reduced resolution mode?*
     L62: Which MIPAS operational mode does this 1.5km vertical resolution correspond to?

Yes. We enhanced the description slightly: *,,We employ here the reduced (or optimised) spectral resolution of 0.0625* cm^{-1} *that was used in the majority of its operational years. Similarly, we employ the vertical sampling of* ≈*1.5* km *in the UTLS being mostly used from 2005 till the end of operation in 2012 (RR27/nominal mode)."*

3.   *L86: a spectral sampling of 1.25cm^{-1} seems very large*

The original PREMIER IRLS was assumed to operate in two different modes; a chemistry mode with a spectral sampling of 0.2 cm^{-1} and a dynamics mode with a spectral sampling of 1.25 cm^{-1} (the spectral resolution after apodization is even worse). The spectral sampling (i.e. interferogram length) was reduced for dynamics mode to enable a higher spatial resolution at the same downlink data rate (which was limited for a variety of reasons). The major primary scientific interest for the dynamics mode were the detection of gravity waves (by means of temperature) and stratosphere-troposphere exchange (CFC-11, O3, and H2O); all these targets could be successfully derived in sophisticated retrieval studies. While this coarse resolution does not allow the resolving of individual lines, it still can be thought of as a highly configurable, and thus much more versatile radiometer.

See also discussion of the first point of referee #1.

4.   *L86: is this +/- 7 deg or +/- 3.5 deg in azimuth?*

We adopted the text to state *,,*±*3.5°"*.

5.   *L128-L129: This is the only mention of aerosols in the paper. Are aerosols assumed to not exist in the simulations shown here? Are their effects assumed negligible and if so to what extent? What about elevated sulfate aerosols in volcanic plumes? What about the potential for aerosol-cloud interaction studies?*

This paper is only concerned with ice clouds, which are the most common small-scale structure with very strong emissions in the UTLS. Other work by some of the authors deals with enhancements of the CI to an Aerosol/Cloud Index for the detection of sulfate aerosol and ash. Such work can, obviously, be immediately combined with the convex hull method. A tomographic extinction retrieval can also be extended in a similar manner by adding more spectral samples in atmospheric windows to distinguish between emitters of different spectral signature.

We focus here on the spatial aspect though. Future work might explore how to derive more information such as microphysical cloud characteristics or different emitters such as nitric acid trihydrate (NAT) PSCs, ash, sulfate aerosol, or dust.

We added a paragraph noting the limitations of the study: *,,The cloud index is also sensitive to an increased aerosol load such as caused by, e.g., volcanic eruptions, wild fires, or dust storms. The highly sensitive altitude-dependent CI-thresholds will certainly also detect enhanced aerosol levels. Using additional detection and classification methods (e.g. Griessbach et al., 2016) can provide a distinction between ice clouds and aerosols with a different spectral signature. The synthetic studies below disregard aerosols for simplicity's sake."*

Later on, we added to the 3-D retrieval from GLORIA data: *We determine a spatially resolved extinction value that does not allow to distinguish between trace gas, ice cloud, or aerosol emission. In the given spectral range, emission from trace gases is negligible compared to that of ice clouds, and we know from closer inspection of spectra and other sources of*

information that there was no strong aerosol load such as generated by an volcanic eruption or biomass burning.

6. *L138: It's not clear here — would the FTS produce data sampled only at the coarse resolution? Is the spectral resolution sufficient to do a good enough job with the gas retrievals? I'm assuming (from L125) that the emissivity growth approximation lookup tables are generated using high resolution line-by-line calculations and spectrally integrated to the coarse resolution. Is that the case? Some more detailed explanation seems necessary.*

The FTS takes interferograms of a certain length, which are processed to spectra of a certain sampling and resolution (the latter also depends on employed apodization). To relate the measured value to actual emissions, this information (and some more) can be used to compute the instrument line shape. The measurement corresponds then to the convolution of the 'real' continuous spectrum with the instrument line shape.

The IRLS in the discussed form would very quickly take interferograms of just 4 mm length, which corresponds to a spectral sampling of 1.25 cm^{-1}. Whether this is sufficient for trace gas retrievals is beyond the scope of this study, but other studies performed during the pre-selection period of EE7 (Kerridge et al., PREMIER Consolidation of Requirements and Synergistic Algorithms (CORSA) Study, Final Report, ESA, 2012) have examined this in great detail and came to satisfactory results for temperature, ozone, water vapour and some CFCs. From personal experience working with GLORIA data at 0.625 cm^{-1}, we see also no problems for processing actual data (compared to a synthetic study). We actually further degrade the spectral resolution of GLORIA by combining neighbouring samples for a faster retrieval, at the cost of some information and a slightly increased susceptibility to systematic errors. The retrieval approach for such a coarse spectral resolution is different compared to that employed for highly resolving instruments such as MIPAS and closer to, e.g., CRISTA or HIRDLS. The paper does not deal with trace gas retrievals and we do not think that this information will help here.

The tables for JURASSIC2 are indeed computed from line-by-line computations, the Oxford RFM model, to be precise. Those calculations were performed on a very fine grid and convolved with the (rather wide) instrument line shape functions.

We added *,,The tables were computed using a line-by-line model (Dudhia, 2017) convolved with the respective instrument line shapes, which for FTS spectrometers depend mostly on the interferogram length and employed apodization."*

7. *L145-L153: Please provide some information on the approximate optical depths corresponding to the CI values 1.1 and 4 and therefore what you mean by thin and thick clouds.*

Unfortunately there is no clear correlation between CI and optical depth in general, as the CI not only depends on the cloud extinction but also strongly on the background temperature and to some degree on trace gas concentrations. These impacts are reflected in the altitude and seasonally variable CI-thresholds for cloud detection. In our very limited CALIOP IRLS simulations, a CI value of 4.0 might correspond to a transmissivity of 0.86 or (optical depth of 0.14) in the atmospheric window at 833 cm^{-1} and a CI value of 1.1 might correspond roughly to a transmissivity of 0.2 (optical depth 1.6) in the atmospheric window.

We added *,,Typical CI values in cloudy conditions are between 1.1 and 6 (Sembhi et al., 2012; Spang et al., 2012, 2015). The lowest detectable extinction from a space based limb emission measurement with the CI in the atmospheric window at 833 cm^{-1}) is of the order of 2×10^{-5} km^{-1} (Sembhi et al., 2012). For IR limb emission measurements the clouds are termed optically thick when the CI profile at and below cloud altitude runs into saturation, which occurs for extinctions of 5×10^{-2} km^{-1} and higher (Griessbach et al., 2016)."*

8. *L172: Maybe explain the concept of a "convex hull"*

We added ,,*The convex hull of a set of points is the smallest convex shape that fully encloses the points.*"

9. *L174: Maybe clarify this a bit better. What I am getting from this is that "below the threshold" means that the CI detection method got triggered. However, the CI detects a spurious cloud at the tangent, but it was triggered by a real cloud well above the tangent.*

This is correct. The CI method detects a cloud along the ray, but cannot say at which point along the ray. As such it is more capable of detecting cloud free spectra for trace gas processing than identifying positions of clouds. As crude approximation one can assume that the cloud is located at the tangent point, which is often, but not always correct.

We have expanded the introduction to the convex hull method: *If the cloud index of a measurement is below the threshold, a cloud has been detected along the line-of-sight of the measurement. But it is not clear where along the measurement the cloud is located. It could be, in theory, in low earth orbit, right in front of the satellite, close to the tangent point, or at any point in between or beyond. As such, the cloud index is better suited for selecting cloud-free measurements for trace gas retrievals than locating clouds. Due to the curvature of the earth, the line-of-sight of a measurement stays longer in the atmospheric layer surrounding the tangent point than those above. This makes it more sensitive to clouds in this layer than the layers above; but the signal of a 'thicker' cloud at a higher layer is still indistinguishable from a signal of a 'thinner' cloud in the tangent layer.*

10. *L181: "A common approximation of the spatial origin of a radiance measurement is assigning it to its tangent point, which is the location along its line-of-sight that is closest to the surface." The radiance measured is the result of the integration along the refracted ray path (which may also involve scattering of radiation into the line-of-sight). The tangent height is just a convenient label to use.*

Indeed. This is meant by "approximation". At least under optically thin conditions, the majority of radiation often stems from the tangent layer, typically shifted to some degree towards the instrument. In the UTLS, the atmosphere is often not perfectly thin anymore such that more and more radiation stems from the side of the ray path that is closer to the instrument.

However, the tangent point is commonly used as approximate origin. Obviously, it may not be the actual origin and if to call it an approximation or a label doesn't matter much in practice. We think it is important to point out that it is a potentially erroneous, but convenient, attribution.

The major advantage, in our eyes, of the extinction retrieval (and to a lesser extent the convex hull) is that it does away with the overly simplifying approximations such as the (in this case necessary) assignment of the radiance to the tangent point and allows inclusion of further instrument properties such as point spread function, etc.

11. *L197-L210: In this section (and everywhere else) it's not clear whether unrefracted or refracted tangent rays are being described. Refraction will cause the actual tangent point to be lowered and move closer to the instrument compared to the geometric (unrefracted) tangent point.*

Tangent points are always computed by JURASSIC2 using refraction. This is straightforward here due to the use of simulated data. Without refraction, significant errors would occur, especially below 15 km. The influence of temperature structure and pressure on refraction is comparatively small, though, such that simple correction methods can be applied to reduce the error to 10's of metres.

We added: *,,JURASSIC2 is also used to compute lines-of-sight and tangent points in this study using a simple refraction scheme by Hase and Höpfner (1999)."*

12. *L216: The first reference to the CI being a "color-ratio" probably should be on L143.*

We moved the first reference upwards as suggested.

13. *L237: Eqn 1: The role of λ_i is not defined. F' is not mentioned.*

We amended the section to include the missing information.

14. *L250: 1/2 orbit in 25 mins or 1 day (typically 14.5 orbits) in 6 hrs.*

We added: ,,*A full day of measurements (for an exemplary 14.5 orbits) would thus consume ≈ 6 hours.*"

15. *L284: What is the optical depth cut-off value?*

A cut off threshold is difficult to define, as it is a gradual descent into full opacity. Please see answer to comment 7. Assuming 1 km thick homogeneous ice clouds the CI profiles start to run into saturation for extinctions of $5\times10^{-2}\,\mathrm{km}^{-1}$ depending on cloud altitude, background atmosphere and cloud particle size. For extinctions of $1\times10^{-1}\,\mathrm{km}^{-1}$ all CI profiles saturate irrespective of the other properties.

Extinction values larger than 0.02 km^{-1} cause a transmissivity of $\approx 10\%$ after only 100 km. This is probably an extinction value that can be retrieved for clouds shorter than that. Values below 0.001 km^{-1} remain 75% transparent up to 300 km (typical length of a ray in a tangent layer) and can be derived without problems. We are in the process of examining the detection capabilities of such cloud retrievals and the usefulness of the derived extinction to determine, e.g., ice water path.

16. *L361: What is the clear-sky optical depth for the lowest tangent height you are considering?*

Actual tangent points values go down to 8 km due to refraction and some LOS-correction in the retrieval. Clear-sky optical path values go from ≈ 0.18 at 8 km over ≈ 0.1 at 9 km to 0.07 at 10 km.

17. *L392: I don't see how the retrieval could distinguish between spatial vs temporal evolution.*

Indeed, this is a problem of the tomography carried out on air planes that is greatly reduced by using a satellite with its much higher speed over ground.

In this particular case, Occam's razor tells us that a cloud close to the aircraft was responsible for the high radiance at all vertical angles (and the viscam for that matter), as the only alternative would be a humongous cloud forming spontaneously further away and disappearing quickly. The retrieval used an unchanging atmosphere as "a priori" knowledge and thus excludes this possibility for right or wrong. But even when assuming temporal change, this explanation is highly unlikely, and as such is discarded similar to many other potential solutions fitting to the measurements, but being physically implausible.

More rigorously, one can compute a "temporal" averaging kernel matrix to deduce the temporal resolution of deduced quantities similar to the spatial resolution (Ungermann et al., 2011). The temporal resolution here is in the order of dozens of minutes with obvious problems. Using this, one can assign a temporal interval to points of the 3-D volume. Given the temporal resolution of available models and observations, this was however not terribly useful, also taking into account that computing the 4-D averaging kernel matrix is only feasible for selected atmospheric samples for practical reasons.

18. *L426: What about evaporation?*

Indeed. Evaporation and condensation are also processes that complicate the comparison. We extended together ,,*In addition, we used the cloud top product from the MODIS instrument that passed over our measurement area in low Earth orbit around 13:08 UTC, which is*

only slightly beyond GLORIA's measurement period, and still reasonably close to compare the
cloud top altitudes. However, the horizontal position might have been shifted due to advection
and small clouds may also appear and disappear due to condensation and evaporation."

References

Carlotti, M., Dinelli, B. M., Raspollini, P., and Ridolfi, M.: Geo-fit approach to the analysis of limb-scanning satellite measurements, Appl. Optics, 40, 1872–1885, https://doi.org/10.1364/AO.40.001872, 2001.

Christensen, O. M., Eriksson, P., Urban, J., Murtagh, D., Hultgren, K., and Gumbel, J.: Tomographic retrieval of water vapour and temperature around polar mesospheric clouds using Odin-SMR, Atmos. Meas. Tech., 8, 1981–1999, https://doi.org/10.5194/amt-8-1981-2015, 2015.

Dudhia, A.: The Reference Forward Model (RFM), J. Quant. Spectrosc. Radiat. Transfer, 186, 243–253, https://doi.org/doi:10.1016/j.jqsrt.2016.06.018, 2017.

ESA: Report for Mission Selection: PREMIER, Tech. rep., European Space Agency, ESTEC, Keplerlaan 1, 2200 AG Noordwijk, The Netherlands, 2012.

Fischer, H., Birk, M., Blom, C., Carli, B., Carlotti, M., von Clarmann, T., Delbouille, L., Dudhia, A., Ehhalt, D., Endemann, M., Flaud, J. M., Gessner, R., Kleinert, A., Koopman, R., Langen, J., López-Puertas, M., Mosner, P., Nett, H., Oelhaf, H., Perron, G., Remedios, J., Ridolfi, M., Stiller, G., and Zander, R.: MIPAS: an instrument for atmospheric and climate research, Atmos. Chem. Phys., 8, 2151–2188, https://doi.org/10.5194/acp-8-2151-2008, 2008.

Griessbach, S., Hoffmann, L., Spang, R., von Hobe, M., Müller, R., and Riese, M.: Infrared limb emission measurements of aerosol in the troposphere and stratosphere, Atmos. Meas. Tech., 9, 4399–4423, https://doi.org/10.5194/amt-9-4399-2016, 2016.

Hase, F. and Höpfner, M.: Atmospheric ray path modeling for radiative transfer algorithms, Appl. Optics, 38, 3129–3133, https://doi.org/10.1364/AO.38.003129, 1999.

Krisch, I., Ungermann, J., Preusse, P., Kretschmer, E., and Riese, M.: Limited angle tomography of mesoscale gravity waves by the infrared limb-sounder GLORIA, Atmos. Meas. Tech., 11, 4327–4344, https://doi.org/10.5194/amt-11-4327-2018, URL https://www.atmos-meas-tech.net/11/4327/2018/, 2018.

Livesey, N., Van Snyder, W., Read, W., and Wagner, P.: Retrieval algorithms for the EOS Microwave limb sounder (MLS), IEEE T. Geosci. Remote. Sens., 44, 1144 – 1155, https://doi.org/10.1109/TGRS.2006.872327, 2006.

Livesey, N. J. and Read, W. G.: Direct Retrieval of Line-of-Sight Atmospheric Structure from Limb Sounding Observations, Geophys. Res. Lett., 27, 891–894, 2000.

Sembhi, H., Remedios, J., Trent, T., Moore, D. P., Spang, R., Massie, S., and Vernier, J.-P.: MIPAS detection of cloud and aerosol particle occurrence in the UTLS with comparison to HIRDLS and CALIOP, Atmos. Meas. Tech., 5, 2537–2553, https://doi.org/10.5194/amt-5-2537-2012, 2012.

Spang, R., Arndt, K., Dudhia, A., Höpfner, M., Hoffmann, L., Hurley, J., Grainger, R. G., Griessbach, S., Poulsen, C., Remedios, J. J., Riese, M., Sembhi, H., Siddans, R., Waterfall, A., and Zehner, C.: Fast cloud parameter retrievals of MIPAS/Envisat, Atmos. Chem. Phys., 12, 7135–7164, https://doi.org/10.5194/acp-12-7135-2012, 2012.

Spang, R., Günther, G., Riese, M., Hoffmann, L., Müller, R., and Griessbach, S.: Satellite observations of cirrus clouds in the Northern Hemisphere lowermost stratosphere, Atmos. Chem. Phys., 15, 927–950, https://doi.org/10.5194/acp-15-927-2015, 2015.

Steck, T., Höpfner, M., von Clarmann, T., and Grabowski, U.: Tomographic retrieval of atmospheric parameters from infrared limb emission observations, Appl. Optics, 44, 3291–3301, https://doi.org/10.1364/AO.44.003291, 2005.

Ungermann, J.: Tomographic reconstruction of atmospheric volumes from infrared limb-imager measurements, Forschungszentrum Jülich, Jülich, URL `http://hdl.handle.net/2128/4385`, Ph.D. thesis, Wuppertal University, 2011.

Ungermann, J., Blank, J., Lotz, J., Leppkes, K., Hoffmann, L., Guggenmoser, T., Kaufmann, M., Preusse, P., Naumann, U., and Riese, M.: A 3-D tomographic retrieval approach with advection compensation for the air-borne limb-imager GLORIA, Atmos. Meas. Tech., 4, 2509–2529, https://doi.org/10.5194/amt-4-2509-2011, URL `http://www.atmos-meas-tech.net/4/2509/2011/`, 2011.

von Clarmann, T., De Clercq, C., Ridolfi, M., Höpfner, M., and Lambert, J.-C.: The horizontal resolution of MIPAS, Atmos. Meas. Tech., 2, 47–54, https://doi.org/10.5194/amt-2-47-2009, 2009.

Cirrus cloud shape detection by tomographic extinction retrievals from infrared limb emission sounder measurements

Jörn Ungermann[1,2], Irene Bartolome[1], Sabine Grießbach[3], Reinhold Spang[1], Christian Rolf[1], Martina Krämer[1], Michael Höpfner[4], and Martin Riese[1]

[1]IEK-7, Forschungszentrum Jülich GmbH, Germany
[2]JARA, Forschungszentrum Jülich GmbH, Germany
[3]Jülich Supercomputing Centre, Forschungszentrum Jülich GmbH, Germany
[4]IMK, Karlsruher Institut für Technologie, Germany

Correspondence: Jörn Ungermann (j.ungermann@fz-juelich.de)

Abstract. An improved cloud index-based method for the detection of clouds in limb sounder data is presented that exploits the spatial overlap of measurements to more precisely detect the location of (optically thin) clouds. A second method based on a tomographic extinction retrieval is also presented. Using CALIPSO data and a generic advanced infrared limb imaging instrument as example for a synthetic study, the new cloud index method ~~is better in detecting the horizontal cloud extent~~ has a better horizontal resolution in comparison to the traditional cloud index and has a reduction of false positive cloud detection events by about 30 %. The results for the extinction retrieval show even an improvement of 60 %. In a second step, the extinction retrieval is applied to real 3-D measurements of the air-borne limb sounder GLORIA taken during the Wave-driven ISentropic Exchange (WISE) campaign to retrieve small-scale cirrus clouds with high spatial accuracy.

Copyright statement. TEXT

1 Introduction

Clouds, and in particular cirrus clouds, play an important part in the radiative balance of the atmosphere. The effect of cirrus clouds in a changing climate is still uncertain even though a change in frequency of occurrence is well established due to a redistribution of water vapour in the troposphere (IPCC, 2007; Heymsfield et al., 2017).

To increase our understanding of cirrus clouds, ~~proper~~ rigorous observations are required on their frequency, occurrence, coverage, particle sizes, number concentration, ice water content, and altitude. To generate a sufficient statistical basis for modelling and validation, global measurements of cirrus clouds are required, which can only be generated by satellite-borne instruments (e.g. Krämer et al., 2020). Owing to the dryness of the upper troposphere, cirrus clouds generate often only weak signatures in observations by remote sensing instruments, especially nadir viewing ones. Our knowledge about clouds has been advanced greatly in recent times by the active lidar Cloud-Aerosol Lidar with Orthogonal Polarization (CALIOP) on Cloud-Aerosol Lidar and Infrared Pathfinder Satellite Observation (CALIPSO; Winker et al., 2009). Due to its active nature,

it is the most highly-resolving and precise satellite instrument with a cirrus cloud product that has been used successfully to create first climatologies (Nazaryan et al., 2008). Other, passive, nadir viewing instruments have often difficulty detecting ultra-thin cirrus or properly determining the top altitude of the clouds with the necessary accuracy to determine, e.g., the radiative effects. While some advances have been made recently, e.g., by Kox et al. (2014), using data from the SEVIRI instrument on
25 MSG (Meteosat Second Generation; Schmetz et al., 2002), these data products currently lack proper error estimates due to the nature of the used classification algorithms. The most sensitive ~~method~~ passive methods to detect cirrus from space are in any case provided by limb observing instruments. As cirrus clouds are typically horizontally more elongated than vertically, a limb-viewing instrument has a longer path within the cloud generating a stronger signal and also a much higher vertical resolution. This is true for both occultation and passive emission measuring instruments. While occultation instruments are
30 even more sensitive, passive instruments have the advantage of a much higher measurement density necessary to generate a profound global statistical basis. A historical disadvantage of limb sounders was a ~~bad~~ poor horizontal resolution compared to nadir viewing ones, but recent developments of tomographic evaluation schemes in combination with proposed instruments with a higher measurement density level the playing field (Griessbach et al., 2020b).

While tomographic retrievals have become state of the art for limb sounders in general ~~(e.g. Steck et al., 2005; Livesey et al., 2006; Christ~~
35 (e.g. Livesey and Read, 2000; Carlotti et al., 2001; Steck et al., 2005; Livesey et al., 2006; Christensen et al., 2015), in-orbit instruments do not oversample extensively; e.g., the MIPAS instrument on ENVISAT (Fischer et al., 2008) was ~~designed to have~~ operated to have in nominal measurement modes non-overlapping ~~line-of-sights~~lines-of-sight in the tangent layer. Tomography was, due to instrument limitations, mostly performed to increase the retrieval accuracy in the presence of gradients in retrieved quantities along the line-of-sight. Hence, this study evaluates the potential capabilities of near-future limb sounders employing
40 imaging detectors with a much higher measurement density, simply called IRLS (infrared limb imaging sounder) in this study. The hypothetical instrument is largely based on the PREMIER IRLS instrument (Process Exploration through Measurement of infrared and ~~millimetre-wave~~ millimeter-wave Emitted Radiation; Ungermann et al., 2010; ESA, 2012) proposed to ESA in the Earth Explorer program.

The cloud index is a well proven method for the detection of clouds in infrared spectra (Spang et al., 2001a, 2008, 2012). We
45 show how the spatial resolution and accuracy of the cloud index method can be improved upon by the so called over-sampling, where limb sounders measure spectra so frequently that the ~~line-of-sights~~ lines-of-sight of succeeding measurements overlap within the tangent layer. In addition to an enhancement of the cloud index method, we also investigate the capabilities of a tomographic extinction retrieval that employs the same techniques also used for the tomographic retrieval of temperature and trace gases. Previous studies have shown that tomographic methods can increase the horizontal resolution of data products
50 gained from limb sounders up to ideally the spacing between consecutive measurements (von Clarmann et al., 2009; Ungermann et al., 2011; Krisch et al., 2018). Here, we want to investigate how that result typically valid for optically thin conditions transfers itself to optically thicker clouds. To complement the work with synthetic measurements, the final part of this paper applies the extinction tomography to evaluate a tomographic measurement of cirrus clouds made by the GLORIA limb sounder (Riese et al., 2014; Friedl-Vallon et al., 2014). This air-borne instrument points in a 90° angle in relation to the heading of its

carrier and has thus a very different measurement geometry compared to along-track-pointing satellite instruments. In this sense it is a very hard test case for the method as this geometry makes the retrieval much more involved and complicated.

This paper is structured as follows. We will first present briefly the employed data products and the models and instruments they were derived from. Section 3 presents the new algorithms and methods that are then studied in depth in Sect. 4. We conclude with a first 3-D tomographic cloud retrieval based on real GLORIA measurements in Sect. 5.

2 Instruments and Data

2.1 MIPAS

The Michelson Interferometer for Passive Atmospheric Sounding (MIPAS; Fischer et al., 2008) was an infrared Fourier-transform spectrometer aboard the ESA satellite Envisat. It measured the spectral range from $685\,\mathrm{cm}^{-1}$ to $2410\,\mathrm{cm}^{-1}$ with a spectral resolution of up to $0.025\,\mathrm{cm}^{-1}$. We employ here the reduced (or optimized) spectral resolution of $0.0625\,\mathrm{cm}^{-1}$ that was used in ~~its last~~ the majority of its operational years. ~~The vertical sampling was~~ Similarly, we employ the vertical sampling of $\approx 1.5\,\mathrm{km}$ in the UTLS being mostly used from 2005 till the end of operation in 2012 (RR27/nominal mode). We assume for the synthetic simulation of MIPAS measurements a horizontal sampling of $420\,\mathrm{km}$ that was used in the period from 2005–2012 and the vertical field-of-view, which has a full-width-half-max of roughly $0.06°$ (equivalent to about $3\,\mathrm{km}$ vertically; e.g., von Clarmann et al., 2003).

2.2 GLORIA and IRLS

The Gimballed Limb Observer for Radiance Imaging in the Atmosphere (GLORIA; Riese et al., 2014; Friedl-Vallon et al., 2014) is an airborne imaging Fourier-transform spectrometer, capable of acquiring more than 6000 interferograms with its 128×48 used detector pixels in less than 2 seconds. This enables it to measure a full atmospheric profile at once. The horizontal dimension across the line of sight is currently only used to increase the signal-to-noise ratio by averaging, but could be exploited as well, e.g., for imaging small-scale cloud structures. The interferogram acquisition time can be adjusted between fast measurements with coarse spectral resolution and slow measurements with a high spectral resolution over the effective spectral range from $780\,\mathrm{cm}^{-1}$ to $1400\,\mathrm{cm}^{-1}$ (Kleinert et al., 2014). The spectral sampling is configurable between $0.625\,\mathrm{cm}^{-1}$ (roughly $2\,\mathrm{s}$ acquisition time) and $0.0625\,\mathrm{cm}^{-1}$ (roughly $10\,\mathrm{s}$ acquisition time). The effective spectral resolution is roughly a factor of two worse than the sampling due to the employed Norton-Beer apodization (Norton and Beer, 1976). A unique feature of GLORIA is its capability to point ~~its detector~~ the instrument towards different directions ~~compared~~ relative to the aircraft heading. This allows for the measurement of airmasses at an angle between $45°$ and $\approx 132°$ with respect to flight direction. By constantly panning the instrument over the available angles, the same airmasses are measured from multiple directions, which enables the tomographic reconstruction of three-dimensional structures (Ungermann et al., 2011; Krisch et al., 2017, 2018). In addition to the IR instrument, there is also a standard camera with three channels (red/green/blue) operating in the visible range that observes a much wider field-of-view.

GLORIA has been operated successfully during multiple campaigns on both the German HALO research aircraft and the Russian M-55 Geophysika. The measurements discussed later were taken on the 18th September 2017 during the Wave-driven ISentropic Exchange (WISE) campaign based in Shannon, Ireland.

The Infrared Remote Limb Sounder (IRLS) is a concept for an Earth-observing satellite instrument that was originally proposed for the 7th ESA Earth Explorer program. It is, effectively, a GLORIA-like instrument in space with a fixed viewing direction backwards compared to its flight direction. This configuration also allows for tomographic 3-D reconstruction of the measured atmosphere. While the PREMIER IRLS offered higher spectral resolutions, we focus here on the spatial capabilities and thus assume a spectral sampling of $1.25\,\mathrm{cm}^{-1}$ and 15 horizontal measurement tracks covering $7\pm3.5°$ as well as an along-track sampling of $50\,\mathrm{km}$. For the vertical sampling, we assume a pixel pitch of $0.014°$, which corresponds roughly to a vertical sampling of $\approx700\,\mathrm{m}$ in the troposphere. These capabilities are in line with those of the GLORIA instrument and thus certainly achievable. They correspond to the 'dynamics mode', which was envisioned to be used for about half of the instrument measurement time; its primary purpose was a high spatial resolution to reveal processes associated with mixing and convective outflow in the UTLS, as well as three-dimensionally resolving gravity waves to determine momentum fluxes driving global circulation systems (ESA, 2012).

2.3 CALIOP

The Cloud-Aerosol Lidar with Orthogonal Polarization (CALIOP; Winker et al., 2007, 2009) is a nadir viewing lidar on the CALIPSO satellite, which is part of NASA's A-train. CALIOP provides high resolution vertical profiles of cloud and aerosol properties with a vertical resolution of $60\,\mathrm{m}$ below $20.2\,\mathrm{km}$ and $180\,\mathrm{m}$ above and an along track resolution of $5\,\mathrm{km}$. We used cloud extinction data from the L2CPro V3.01 product files (CALIPSO, 2018) of the full month of December 2009 to generate test cases of realistic 2-D cloud scenes for the limb viewing geometry using a radiative transfer model (see Sec. 3). In addition to the given extinction values, we also used a data set where we reduced the supplied extinction values by an order of magnitude. This allows us to explore the sensitivity of limb sounders with respect to clouds that are thinner than those present in CALIOP level 2 products.

2.4 ECMWF

For pressure and temperature in the cloud scene simulations based on CALIOP data and as a priori in all retrievals, ERA-Interim data provided by the European Centre for Medium-Range Weather Forecast (ECMWF; Dee et al., 2011) was employed. The model data is available in $6\,\mathrm{h}$ time steps with the T255/L60 resolution, which corresponds to a horizontal sampling of $\approx80\,\mathrm{km}$. Quadri-linear interpolation is used for resampling the model onto the needed grids, whereby pressure is interpolated in log-space. The horizontal wind speeds and diabatic heating rates from the ECMWF ERA-Interim data were also used for the calculation of backward trajectories using CLaMSthe CLaMS model introduced in the next section.

4

2.5 CLaMS-ICE

As CALIOP only provides vertical 2-D slices, we turned towards simulations generated by the Chemical Lagrangian Model of the Stratosphere (CLaMS; McKenna et al., 2002; Konopka et al., 2007; Ploeger et al., 2010) for providing realistic 3-D cloud structures. The CLaMS-ICE module (Luebke et al., 2016) includes a double-moment bulk microphysics scheme for modelling cirrus clouds (i.e. ice water content and ice crystal number; Spichtinger and Gierens, 2009). The box model runs in forward direction on backward trajectories (24 hours) started from points on a regular grid with user-defined resolution and extent in longitude, latitude, and pressure space. A resolution 0.25° in the horizontal and 0.5 km in the vertical domain is used for resolving finer cirrus structures compared to the original ~~ERA interim~~ ERA-Interim resolution. For ~~initialisation~~ initialization, cloud ice water content and specific humidity from ~~ERA interim~~ ERA-Interim are spatially interpolated to the CLaMS-ICE starting point of each individual trajectory.

The trajectories are calculated on hybrid-potential temperature coordinates, which allows to resolve transport processes in the troposphere influenced by the orography and transport processes in the stratosphere, where adiabatic horizontal transport dominates.

To reduce the computational effort of the radiative transfer model, we transform the ice water content and radius information supplied by the CLaMS-ICE module to a simple extinction coefficient by the formula of Gayet et al. (2004): $E = A \cdot I \cdot R^{-1}$, with E being extinction in $\mathrm{km^{-1}}$ at 804 nm, $A = 1500\,\mathrm{mm^3 g^{-1}}$, I the ice water content in $\mathrm{g m^{-3}}$, and R the radius of particles in µm.

3 Methods

3.1 JURASSIC2

This paper employs the JUelich RApid Spectral Simulation Code version 2 (JURASSIC2), which is a radiative transfer code optimized for large-scale and tomographic simulations and retrievals (Hoffmann, 2006). It includes capabilities from computing spectrally resolved radiances line-by-line to using spectrally averaged lookup-tables for extremely fast computations. The algorithmic adjoint model allows its efficient use in retrieval schemes (employing the JUelich Tomographic Inversion Library; JUTIL) and data assimilation in general. JURASSIC2 has been exemplary used for the analysis of CRISTA-NF data (e.g. Kalicinsky et al., 2013), for the study of clouds and aerosol using MIPAS data (e.g. Griessbach et al., 2013, 2014), for the operational processing for the GLORIA instrument (Ungermann et al., 2015, e.g.) and for studies on the aerosol layer in the Asian Summer Monsoon (Höpfner et al., 2019).

In this study, the emissivity-growth-approximation (e.g. Weinreb and Neuendorffer, 1973; Gordley and Russell, 1981) is used in combination with pre-calculated ~~lookup tables~~ lookup-tables of optical path (also called optical depth, or thickness) in relation to temperature, pressure, and volume mixing ratio to quickly compute radiances and derivatives with respect to temperature in a discrete representation of the atmosphere. The tables were computed using a line-by-line model (Dudhia, 2017)

5

convolved with the respective instrument line shapes, which for FTS spectrometers depend mostly on the interferogram length and employed apodization.

JURASSIC2 is also used to compute lines-of-sight and tangent points in this study using a simple refraction scheme by Hase and Höpfner (1999).

Simulations with JURASSIC2 for MIPAS-like and IRLS spectra employed the trace gasses CCl_4, $CFC-11$, H_2O, HNO_3, and O_3 with climatological values (Remedios et al., 2007). A ray-tracing step length of $5\,km$ was employed. For both MIPAS-like and IRLS measurements, the spectral samples from $787.50\,cm^{-1}$ to $796.25\,cm^{-1}$ and from $831.25\,cm^{-1}$ to $835.00\,cm^{-1}$ were used, albeit with different spectral sampling for each instrument of $0.0625\,cm^{-1}$ and $1.25\,cm^{-1}$, respectively, and a strong Norton-Beer apodization (Beer, 1992). We simulated synthetic MIPAS-like and IRLS radiances for all CALIOP extinctions of December 2009 and these microwindows.

3.2 Cloud index

A practical method for identifying a radiance measurement of a cloud is the so called cloud index (CI), first introduced by Spang et al. (2001b). The CI is a color ratio, defined as the ratio between the radiance averaged over a spectral region with a strong emission feature, such as the CO_2 Q-branch at 12.6 μm~~and~~, and the radiance averaged over an atmospheric window, such as the one located at 12 μm. It is a dimensionless quantity with a slight dependence on latitude and season. For given tangent point altitudes, one can derive specific thresholds that separate cloudy measurements from others. Typical CI values in cloudy conditions are between 1.1 and ~~4 (Spang et al., 2012, 2015) indicating optically thick to thin conditions~~6 (Sembhi et al., 2012; Spang et al., 2012, 2015). The lowest detectable extinction from a space based limb emission measurement with the CI in the atmospheric window at $833\,cm^{-1}$) is of the order of $2 \cdot 10^{-5}\,km^{-1}$ (Sembhi et al., 2012). For IR limb emission measurements the clouds are termed optically thick when the CI profile at and below cloud altitude runs into saturation, which occurs for extinctions of $5 \cdot 10^{-2}\,km^{-1}$ and higher (Griessbach et al., 2016). Here, we employ altitude dependent thresholds of Sembhi et al. (2012) to determine if an index indicates a cloud. For optically thin conditions, the CI correlates well with extinction and the integrated volume density or area density path along the limb path (Spang et al., 2012). Latter differentiation depends on the particle radius range, where larger median radii, typical for ice clouds, correlate with the area density. Although the CI approach is an effective and computational cheap detection mechanism for thin and thick clouds, its information content is limited when retrieving cloud information below the cloud top, as clouds affect the CI of clear air below and hence, the cloud detection thresholds are not effective in distinguishing clear air from cloud below the cloud top.

The cloud index is also sensitive to an increased aerosol load such as caused by, e.g., volcanic eruptions, wild fires, or dust storms. The highly sensitive altitude-dependent CI-thresholds will certainly also detect enhanced aerosol levels. Using additional detection and classification methods (e.g. Griessbach et al., 2016) can provide a distinction between ice clouds and aerosols with a different spectral signature. The synthetic studies below disregard aerosols for simplicity's sake.

3.3 Cloud extent retrieval

This section describes two different approaches to the spatial detection of ice clouds from measured infrared limb spectra. The first approach builds on the CI method (e.g. Spang et al., 2012), which can detect the presence of a cloud in a measured spectrum. Previous satellite instruments, such as MIPAS-Envisat (Fischer et al., 2008), have a comparatively coarse measurement pattern, where individual lines-of-sight of measured spectra do not ~~meaningfully~~ usefully intersect (at least in the most common operation modes). Figure 1 shows the ~~line-of-sights~~ lines-of-sight of measurements of a MIPAS-like instrument and the assumed IRLS. At lower altitudes, the ~~line-of-sights~~ lines-of-sight of MIPAS do not overlap at all in the tangent layer. In contrast, the IRLS has a very fine measurement grid, where many ~~line-of-sights~~ lines-of-sight overlap to the extent that the ~~line-of-sights~~ lines-of-sight of the immediately neighboring measurements of one altitude overlap at their tangent point altitude. This overlap of the IRLS lines-of-sight allows for the application of tomographic methods (e.g. Carlotti et al., 2001; Livesey et al., 2006) and even requires them to utilize the instrument to its full capacity.

The first proposed spatial detection method is a two-dimensional evolution of the CI method, described in Sec. 3.3.1. The cloud detection is improved by taking into account not only the tangent point of a measurement but instead the full extent of and overlap within the tangent point layer. This extension already allows for the exploitation of the increased sampling density of IRLS like instruments.

In addition, a much more computationally involved method is proposed in Sec. 3.3.2. This method deduces the atmospheric extinction values of clouds in a tomographic non-linear inversion that has so far been mostly used to derive temperature and trace gas concentrations.

3.3.1 2-D convex hull CI

~~The principal problem of the CI method is that one does not know at which point of the~~ If the cloud index of a measurement is below the threshold, a cloud has been detected along the line-of-sight of the measurement. But it is not clear where along the measurement the cloud is located. It could be, in theory, in low earth orbit, right in front of the satellite, close to the tangent point, or at any point in between or beyond. As such, the cloud index is better suited for selecting cloud-free measurements for trace gas retrievals than locating clouds. Due to the curvature of the earth, the line-of-sight of a measurement ~~a potential cloud is located. Sometimes even a cloud far above the tangent point layergenerates a CI value below the threshold.~~ stays longer in the atmospheric layer surrounding the tangent point than those above. This makes it more sensitive to clouds in this layer than the layers above; but the signal of a 'thicker' cloud at a higher layer is still indistinguishable from a signal of a 'thinner' cloud in the tangent layer.

This section introduces a method that exploits the existing overlap of measurements of limb sounder instruments to address this problem and improve upon the positioning of detected clouds, i.e. to properly compute the convex hull of clouds determined by the CI of individual spectra. The convex hull of a set of points is the smallest convex shape that fully encloses the points. As the CI is computed from integrated micro-windows over a rather large spectral range, there is no meaningful effect on the results by the spectral resolutions of IRLS measurements. Therefore, this aspect of the different instruments is neglected

(further, the increased spectral resolution typically comes at the cost of a reduced horizontal sampling, which counteracts the purpose of exploring the spatial detection capabilities).

A common approximation of the spatial origin of a radiance measurement is assigning it to its tangent point, which is the location along its line-of-sight that is closest to the surface. This is the location where the air is densest and thus from where most radiation is emitted in optically thin conditions. Obviously, this assumption breaks down in the presence of clouds. This poses the largest problem in determining the position of clouds from the CI and the tangent point location alone. Figure 2 shows an extinction ~~cross-sections~~ cross-section and associated CI values. Comparing the location of small clouds (extinctions $> 10^{-3}\,\mathrm{km}^{-1}$) in the upper panels to the corresponding structures in CI in the lower panels, one can easily see how the assumption of emission stemming from the tangent point breaks down for an optically thick (i.e., intransparent) medium. The curved structures peak at the location of the cloud and then extend downwards to both sides for measurements that either 'hit' the cloud before or after the tangent point. The resulting structure is still useful as it is a strict overestimate of the dimensions of the clouds (above the detection limit). Also the cloud top altitude of the true cloud can be properly determined to high accuracy compared to, e.g., nadir sounders.

Exploiting that measurements indicated as cloud free according to the CI have typically no cloud within the tangent point layer, where the lines-of-sight are nearly horizontal, we can improve the method. Especially optically thin ice clouds are often rather thin vertically, which means that the radiances measured by lines-of-sights passing through the thin cloud at steeper angles may not be strongly affected and thus not detect its presence. Therefore, one may not easily extend the cloud-free assumption to the layers that the line-of-sight passes through at altitudes significantly above the tangent altitude.

The proposed first new detection method works as follows:

1. Build a regular grid covering the cross-section. Here, a grid with a vertical spacing of 500 m was chosen to be a bit finer than the measurement grid of the IRLS to be robust against slight variations of tangent point altitude due to temperature and pressure variations. The horizontal location of the profiles was taken to coincide with the lowermost tangent points (this causes a slight shift between grid and tangent point location for higher altitudes). Each grid box is assigned a value of 0 (i.e. is assumed to be cloudy; final values of zero can also be used, however, to determine grid boxes without measurement information).

2. The line-of-sight for each spectrum is computed for a distance of $d\,\mathrm{km}$ before and behind its tangent point. Here, a very conservative (small) value of 100 km was chosen for d to reduce the number of false-negatives (i.e., to decrease the number of undetected clouds).

3. Successively for each line-of-sight, each grid box that it passes through is assigned the maximum between its current value and the CI of the spectrum.

4. Last, the CI of each grid box is compared to the CI threshold associated with its altitude and latitude band (Sembhi et al., 2012) to determine whether or not a cloud is present.

This algorithm gives a cloud/no-cloud decision for the 2-D cross-section measured by the limb sounder that is more precise than the CI method alone. For one cross-section of a half-orbit as shown below (e.g., Fig. 4), the method uses less than 1 minute

245   of computation time on one core of ~~a current system~~an AMD EPYC 7351P 16-Core Processor operating at 2.9 GHz.

3.3.2 Tomographic extinction retrieval

The second method investigates briefly into the capabilities of employing a full-blown non-linear retrieval for the determination of cloud positions. This is a computationally more demanding task compared to the color-ratio based schemes and as such may be less suited for a quick identification scheme for filtering affected spectra. However, computational capacity steadily increases

250   and the current scheme is well suitable for real-time usage.

The method is comparable to the one employed by Castelli et al. (2011), but simplified due to the neglecting of scattering. The intent is to show the capabilities of this approach in combination with an increased measurement density. The retrieval employed the same JURASSIC2 forward model and setup that was used for generating the synthetic measurements. While the simulated measurements were generated using the original, fine grid on which the CALIOP L2 data are supplied, the retrieval

255   grid was reduced to 500 m vertically in the relevant altitude range and $\approx$20 km horizontally. This corresponds to roughly 1000 profiles for the half-orbit in the CALIOP based simulations. We use the same spectral setup as used for the generation of synthetic radiances, i.e. only two averaged radiances were simulated centered at ~~796.25~~792.00 cm^{-1} and ~~835.00~~833.00 cm^{-1}. The same trace gases and volume mixing ratios were used in the retrieval as in the forward simulation. Perfect knowledge was assumed for all trace gases, obviously a strong simplification. But due to the strong radiative effect even of thin ice clouds in the

260   limb, this is likely justified, but beyond the scope of this study to examine. Temperature and extinctions were assumed unknown and climatological values and a zero profile were used as a priori and initial guess for temperature and extinction, respectively. Also, the scattering effect of clouds was neglected here, as we are interested only in the detection, not in a quantitative analysis of the retrieved extinction.

Computing the spatially located extinction from the radiances poses an inverse problem. The solution to this problem is

265   identified by iteratively modifying an atmospheric state $\boldsymbol{x}_i$, $i \in \mathbb{N}_0$, such that the simulated measurements $F(\boldsymbol{x}_i)$ progressively agree better with the actual (in this case also partially simulated) measurements $\boldsymbol{y}$ within expectation to the noise equivalent spectral radiances (NESR) of the measurements under the side-condition of being close to a 'plausible' atmospheric state $\boldsymbol{x}_\mathrm{a}$:

$$
\begin{aligned}
\boldsymbol{x}_{i+1} \;=\; & \boldsymbol{x}_i - \left(\mathbf{S}_\mathrm{a}^{-1} + \mathbf{F}'(\boldsymbol{x}_i)^\mathrm{T} \mathbf{S}_\epsilon^{-1} \mathbf{F}'(\boldsymbol{x}_i) + \lambda_i \mathbf{I}_n \right)^{-1} \cdot \\
& \left(\mathbf{S}_\mathrm{a}^{-1} (\boldsymbol{x}_i - \boldsymbol{x}_\mathrm{a}) + \mathbf{F}'(\boldsymbol{x}_i)^\mathrm{T} \mathbf{S}_\epsilon^{-1} \left(\boldsymbol{F}(\boldsymbol{x}_i) - \boldsymbol{y} \right) \right).
\end{aligned}
\tag{1}
$$

270   The matrix ~~$\mathbf{S}_\epsilon$ is set up assuming a 0.1 % error in radiance. The matrix~~ $\mathbf{S}_\mathrm{a}^{-1}$ is defined as a Tikhonov-Phillips type regularization matrix imposing smoothness conditions in horizontal and vertical direction on the solution (Tikhonov and Arsenin, 1977). The parameter λ is a dampening parameter of the Levenberg-Marquardt-algorithm and typically strives to zero as $\boldsymbol{x}_i$ converges on the solution (Levenberg, 1944). $\mathbf{F}'(\boldsymbol{x}_i)$ denotes the Jacobian matrix of F evaluated at $\boldsymbol{x}_i$. Typically, one uses $\boldsymbol{x}_a$

as value for x_0. The matrix $\mathbf{S}_\epsilon$ is set up assuming a 0.1 % error in radiance, which has been chosen to allow for differences caused by the use of different grids for generating the synthetic measurements and the retrieval itself.

For temperature, only the second ~~derivative is~~ derivatives are constrained with correlation lengths of vertically 1 km and horizontally 200 km. Restraining the second derivative enforces a smooth lapse rate for temperature (Ungermann et al., 2015), which is useful for further analysis of the dynamical structure around the thermal tropopause. For extinction, the first ~~derivative is constrained~~ derivatives in both spatial directions are constrained using the same correlation lengths in addition to ~~a weak regularization~~ imposing a weak constraint of the absolute extinction values towards the zero profile. These values are selected to be similar to those practically used in tomographic studies for the GLORIA instrument. The qualitative result does not depend largely on the type of regularization as long as it is neither too strong to ~~smoothen~~ smooth the solution nor too weak to allow ~~for~~ oscillations, as the aim is so far not to perfectly reproduce the original extinction values, but to arrive at a simple cloud/no-cloud product. The retrieval employs the numerical techniques developed for the GLORIA limb sounder tomography to quickly derive a solution (Ungermann et al., 2010, 2011). As only 2 spectrally averaged samples are simulated from each spectrum, the computation time and memory consumption are manageable. The retrieval for a half-orbit consumes about 200 ~~MiB~~ MB, mostly for storing Jacobian matrices and requires about 25 minutes on 8 cores (same machine as above) to converge to a satisfactory state, which can be readily accomplished in real-time. A full day of measurements (for an exemplary 14.5 orbits) would thus consume $\approx$6 hours.

4 Study on synthetic data

In this section we use synthetic spectra generated by JURASSIC2 based on CALIOP extinctions to evaluate the algorithms. To focus on the relative capabilities of the algorithms, we added Gaussian noise to simulated MIPAS or IRLS measurements with a standard deviation of 0.8 nW cm^{-2}sr^{-1}cm.

4.1 2-D convex hull CI

In a first step, we compare the cloud indices as gained from MIPAS-like and IRLS spectra. Figure 2b shows the CI for the simulated spectra based on an exemplary CALIOP cross-section and the MIPAS measurement grid and spectral resolution. The simulated radiances were generated using the grid defined by the CALIOP L2 data shown in Fig. 2a. ~~It is obvious that the~~ The 'pixels' ~~are rather~~ corresponding to MIPAS measurements in Fig. 2b are very coarse compared to the fine structure of the clouds contained in the CALIOP data due to the much sparser horizontal sampling density of the MIPAS instrument. Figure 2c shows the IRLS simulations. The increased spatial sampling density results in a much finer sampling of the clouds, but the bow-like artifacts due to the optically thick atmospheric conditions become apparent. These are also given in the synthetic MIPAS data but barely discernible due to the coarse measurement grid. Figures 2d-f show the same situation, but with CALIOP extinction reduced by a factor of ten. These numerical experiments shift the focus to very thin clouds that may not be present in the original data set.

305   The results of the convex hull CI algorithm are exemplary depicted in Figs 3 and 4. Figure 3 shows the results for the MIPAS instrument, while Fig. 4 shows the result for the IRLS instrument. For MIPAS, no obvious differences between CI and convex hull CI are apparent. The minor visible discrepancies can be attributed to the difference between the tangent point grid of the CI and the rectilinear grid on which the convex hull CI algorithm operates. In contrast, a noticeable improvement can be seen for the IRLS measurements. The convex hull CI algorithm reduces the bow like structures around thin clouds. Especially the

310   comparatively small structures at 38°N have a much reduced ~~sized~~ size more aligned with the true structure as shown by the extinction contour. But a deficit is also apparent. Below thick clouds, no actual measurement information is present and the CI is (wrongly) attributed at the tangent point location. This will still cause an overestimation of cloud presence.

4.2 2-D tomographic extinction retrieval

This section presents some results of the extinction retrieval. Figure 5 shows the extinction retrieved for the same extinction

315   distribution derived from CALIOP data for MIPAS and IRLS data for one of the 440 processed cross sections. Both retrievals were setup identically with the difference that Fig. 5b used simulated MIPAS measurements and a coarser horizontal ~~resolution~~ retrieval grid ($\approx$160 km) and Fig. 5c used simulated IRLS measurements. The MIPAS-based retrieval is both horizontally and vertically coarser in comparison to the IRLS retrieval as required by the different measurement grid. The results are generally more accurate than the picture provided by the CI in Fig. 3 as even for the coarse MIPAS measurement grid, the

320   overlap of measurements at higher altitudes can be used to constrain the location of thin clouds better. The retrieval using the IRLS measurement specification in Fig. 5c offers a much better resolved result. The ~~higher~~ finer spatial sampling and the reduced ~~FOV~~ field-of-view allow us to see below clouds with clear sky conditions as with the equatorial high cirrus cloud. We encountered similar conditions also with our air-borne instruments GLORIA (see below) and CRISTA-NF (Spang et al., 2008). The location of clouds, expressed in increased values of extinction, is more precise and much closer to the actual extinction

325   distribution compared to the CI based methods. Some artifacts remain below thick clouds, where, due to their opacity, no or ~~next to~~ nearly no measurement information is present. As such the values below 9 km at 20°S are not reliable. On the other hand, the weak structures at and above 15 km are well reproduced. Obviously, the retrieval works better for optically thin conditions.

4.3 Comparison of 2-D cloud top detection accuracy

330   This section aims to quantify the performance of the 2-D convex hull CI and the 2-D tomographic extinction retrieval algorithms with respect to cloud top height estimation. We focus here on the capabilities of the IRLS instrument. Figure 6 shows an exemplary CALIOP orbit with detected cloud extent according to the CALIOP extinctions (extinction larger than $10^{-4}\,\mathrm{km}^{-1}$), cloud index (CI), convex hull cloud index (convex hull CI) and tomographic extinction retrieval (extinction larger than $3 \cdot 10^{-4}\,\mathrm{km}^{-1}$). A slightly larger threshold is employed here, as the smoothing by the regularization extends the

335   rather large extinctions vertically and a smaller threshold would thus lead to a systematic overestimation of cloud extent. One can immediately see that all methods typically agree within about 1 km, with larger errors occurring at the border of extended cloud regions.

11

Table 1 shows the numerical results for the cloud top height derived by the three algorithms for 440 semi-randomly selected CALIOP orbits (we arbitrarily picked one month of data). Using unmodified CALIOP extinctions, the CI shows a positive bias of 1.08 km with a standard deviation of 2.29 km. There are two major sources for a high bias. First, the field-of-view of the instrument causes an overestimation of cloud top altitude, especially for thicker clouds (e.g. Griessbach et al., 2020a). Second, and more importantly, the cloud is horizontally extended causing cloud detection events beside the actual cloud, where no cloud is in the original data (e.g. Kent et al., 1997). The second effect mainly causes the large variance in the results. As expected, the convex hull CI algorithm significantly reduces this bias, whereby the tomographic extinction retrieval seems to be even superior. Both are capable of reducing the impact of "horizontal cloud lengthening". For thinner clouds, the situation improves all around. Using clouds that are an order of magnitude thinner, here, the CI shows a bias of only 0.66 km. For optically thinner clouds the general cloud top height overestimation is reduced or even turns into an underestimation (Griessbach et al., 2020a) and the "horizontal cloud lengthening" is also reduced (Fig. 5). The bias of the convex hull CI algorithm and the tomographic extinction retrieval are both ~~in~~ on the order of 160 m, whereby the extinction retrieval has a reduced standard deviation compared to the convex hull algorithm.

As the overestimation of the horizontal extent of clouds strongly affects the cloud top altitude comparison, we examined more closely how well the shape of the cloud top is reproduced. In a first step the true cloud top is determined from CALIOP extinctions. Using the tomographic extinction retrieval grid, all cloud top grid boxes plus all boxes within two squares distance (Manhattan norm, ± 1 km vertically, ± 50 km horizontally) are selected for comparison. The results are collected in Tab. 2. The table shows an increase for correctly identified cloudy pixels for the three methods with the conventional CI being worst and the tomographic extinction retrieval being best. False positives decrease accordingly. However, there is a slight increase for false negatives, which is caused by horizontally small clouds that are filtered away by the convex hull CI as the CI is pushed below the threshold and for which the tomographic extinction retrieval determines an extinction below the threshold (potentially due to slightly smearing out the cloud). This is asserted by the numbers for the scaled extinction test cases, where the amount of false negatives increases over the board

4.4   3-D IRLS scenario — Spatial detection capabilities

This section describes the result for the convex hull algorithm CI for the CLaMS-ICE model based simulations that allow the simulation of the across-track coverage of the IRLS instrument in contrast to the CALIOP based simulations that allow only a simulation of the center track.

Figure 7 shows horizontal cross-sections at several pressure levels through the extinctions derived from the 3-D CLaMS-ICE ice water content simulation. The center of the simulated IRLS measurements follows the 19°W meridian. Actual satellite measurements of the instrument will not follow a perfect polar orbit, but for the simulations, the difference is negligible and simplifies the simulation setup. One can see a cloud field on the left-hand-side on lower altitudes and a second cloud field on the right-hand-side at different altitudes. At higher latitudes, the two cloud fields merge. This situation gives a nice across-track variation over the images of the IRLS that can be examined in the following.

This variation can be better seen in Fig. 8 that shows the CLaMS-ICE extinction as 'images' as the IRLS would see it. Each 'pixel' of the picture corresponds to one pixel of the IRLS, but the horizontal coverage is slightly larger by 2 pixels. The IRLS would take roughly twice as many images of the situation than depicted here. The depicted images cover the latitudes from 39.1°N to 64.6°N. The simulation ends shortly beyond these latitudes. The images show a two-layered structure on the left-hand-side between 42.7°N and 51.9°N. Northward of 46.4°N one can see the second cloud structure to the right with first rather faint extinctions and then higher ones until the two ~~structure~~ structures join around 61°N.

The measurements of the individual tracks can be treated individually as singular cross-sections and may be assembled in a second step. As MIPAS only measured a single track, no MIPAS simulations are shown here for comparison as the results will not be different from those of Sect. 4.1.

The computation of the conventional CI and the application of the cloud index threshold is depicted in Fig. 9a and b. Similar to the simulations of Sect. 4.1, the cloud extent is overestimated to the sides of the clouds and below. The result of the convex hull CI algorithm is shown in Fig. 9c and d. One can see again, that the new algorithm follows the true extinction closer. In the case of the central track (Fig. 9e), it becomes apparent that the chosen value for extinction of $10^{-3}\,\mathrm{km}^{-1}$ is not the true detection limit as the faint cloud structure in the center track below that limit is also detected by the CI.

The individual tracks can then be assembled into a three-dimensional view on the cloud structure. Figure 10a shows a three-dimensional representation of the true extinction distribution. The zonal extent is limited by the measurement coverage of the IRLS. One can see the across-track and along-track variation as well as the vertical structure. The result of the convex hull CI algorithm is presented in Fig. 10b. The three-dimensional results agree similarly as the cross-sections discussed before. The cloud extent is slightly overestimated horizontally and the vertical structure of the cloud is lost, respectively, the bottom of the cloud is often located lower than in the actual extinction structure. Also, the very small spot of a cloud to the south was not detected.

5 3-D retrievals using GLORIA measurements

The final section applies the extinction retrieval approach on real measurements. While currently no limb sounding satellite instrument with a sufficient measurement density in the UTLS exists, the airborne GLORIA instrument can serve well for a feasibility study, even though the 3-D retrieval of GLORIA is more complicated than the one needed for satellite-borne instruments. In fact, it resembles more closely techniques to reconstruct 3-D cloud structures from ground based cloud imagers (Mejia et al., 2018), but with a horizontal viewing geometry and a moving single instrument instead of multiple stationary ones. We determine a spatially resolved extinction value that does not allow to distinguish between trace gas, ice cloud, or aerosol emission. In the given spectral range, emission from trace gasses is negligible compared to that of ice clouds, and we know from closer inspection of spectra and other sources of information that there was no strong aerosol load such as generated by a volcanic eruption or biomass burning.

This numerical experiment uses measurements acquired on the 18th September 2017 during the WISE campaign. Here, the GLORIA instrument operated with a spectral sampling of $0.2\,\text{cm}^{-1}$ and panning from $45°$ to $132°$ in $6°$ steps, while following a straight flight path.

405 We used all ~~measurements~~ images taken between 11:10 UTC and 12:35 UTC in the reconstruction. ~~All spectral samples between 832.4 and 834.4~~ The 3-D retrieval is computationally significantly more expensive compared to the 2-D retrievals as the number of unknowns is much higher and the involved algorithms scale with a power of given unknowns. The atmospheric volume is also much less constrained by the measurements as the number of unknowns vastly outnumbers the measurements and the distribution of information is far from homogeneous. We found that deriving temperature and extinction similar to

410 the 2-D setup works well within the volume covered by tangent points, but quickly deteriorates outside. Thus, we neglect the temperature retrieval here, as this improved the retrieval on three fronts. First, this allows discarding of the $792\,\text{cm}^{-1}$ ~~were averaged and used as single micro-window for the extinction retrieval. We used only a single window here, as we assumed that ECMWF supplies temperature with a sufficient quality such that we do not need to retrieve it. We further drastically simplify the retrieval by not taking~~ window and to not take any trace gas emissions into account in the forward modelling, drastically

415 improving the forward model speed by orders of magnitude. Second, it halved the number of unknowns, thereby increasing convergence speed of iterative solvers by a factor of roughly four and decreasing memory consumption by half. Third, this also stabilized the extinction retrieval such that the extinction values outside the core volume are less affected by retrieval artifacts. The employed single microwindow averaged all spectral samples between $831.2\,\text{cm}^{-1}$ and $835.0\,\text{cm}^{-1}$ (GLORIA operated in a mode that allows for a spectral sampling of $0.2\,\text{cm}^{-1}$ during this portion of the flight). Measurements with tangent points below

420 $\approx 9\,\text{km}$ altitude were discarded as they do not contribute to the reconstruction of the cirrus clouds at higher altitudes. Thus, 629 separate images with in total 61 611 radiance values were employed in the retrieval. Figure 11 shows one exemplary cloud scene. While the camera in the visible samples a viewing angle of about $11°$ and shows an extended cirrus cloud at $\approx 10.5\,\text{km}$, the infrared camera samples only a section of about $1.5°$. Here, the employed horizontal averaging over the IR pixels is useful, but other imaged clouds exhibit finer structures within an image, similar to the filament at $319.3°$ azimuth. But, even with the

425 fine retrieval grid described below, they would remain inaccessible. Future work would encompass a measurement scheme that reduces the horizontal gaps between images and exploits the full resolution capabilities of the detector.

The retrieval grid used a vertical sampling of $125\,\text{m}$ and a horizontal sampling of $10\,\text{km}$ in both horizontal directions. The grid is rectilinear in a stereographic projection centered around the center point of the volume rotated in such a fashion that one axis of the grid is parallel to the flight path. The grid covered the volume of $\pm 1\,000\,\text{km}$ in the horizontal direction and between

430 $8\,\text{km}$ and $16\,\text{km}$ altitude in the vertical direction. The grid was extended further to encompass the whole measured volume up to $64\,\text{km}$ altitude at a reduced sampling[1]. Altogether, this resulted in 3 235 925 extinction values to be reconstructed. This number is significantly larger than the number of measurements, making this a drastically under-determined problem.

~~To compensate for the under-determination, we employed regularization~~ The inverse problem, i.e., identifying an atmospheric state fitting to the measurements, is an ill-posed problem. To solve it, we approximate it by a well-posed, regularized formulation.

435 To regularize the problem, we employ constraints of zero-th and first order. We used a standard deviation for extinction of

---

[1]vertically, 2 km steps until 24 km, 8 km steps until 64 km; horizontally, 1000 km steps until 3 000km distance from the center

$10^{-3}\,\mathrm{km}^{-1}$ for atmospheric samples with an ECMWF potential vorticity below 3 PVU and $5 \cdot 10^{-5}\,\mathrm{km}^{-1}$ for atmospheric samples with an ECMWF potential vorticity above 5 PVU. In between a linearly interpolated value was used. This setup avoids strong cloud signals in the stratosphere, which might otherwise appear as artifacts outside the well-measured volume and it doesn't affect the reconstructed extinctions in the well-resolved region. We assumed extinction structures to be typically

440 $\approx$100 times longer horizontally than vertically and scaled the first derivative accordingly. The well-resolved volume surrounds the locations of the tangent points and is highlighted in the retrieval results. See Krisch et al. (2018) for a more involved discussion on this kind of linear-flight tomography and its capabilities.

Figure 12 shows the measured brightness temperatures of the averaged microwindow used in the retrieval taken at different azimuth angles. Just ~~the~~ these three given angles give already some insight into the real cloud structure (while the retrieval has

445 also access to the full set of angles). The thin structure at 10.5 km at 11:45 UTC in Fig. 12a is the increased radiance emitted by a cirrus cloud. From this figure alone, it is not determined if the cloud extends vertically over several kilometres or moves away from the aircraft at earlier measurements. The images taken at different azimuth angles deliver the missing information. The image taken at 126° shows the cloud ~~shrunken~~ shrunk to nearly a single blob. This tells us the angle of the elongated cirrus cloud with respect to the flight path. Taken together, we can compute that this cloud runs nearly in a perfect North-South

450 direction. In combination with the slanted structure of the cloud at other angles the horizontal extent orthogonal to the flight path can be computed. Further information could be discerned from the vertical structure at 11:45 UTC in Fig. 12b. A similar structure is given in all measurements taken at this time. This is caused by a cloud very close to the aircraft as it is seen at all azimuth angles around this same time, but not present at times more than a couple of minutes before and after. The retrieval is a mathematical method to extract this and more information from the measurements in an optimal fashion.

455 The volume can best be reconstructed close to the tangent points of the radiance measurements (e.g. Krisch et al., 2018). Atmospheric samples much closer to the flight path were not measured at all. Atmospheric samples beyond the volume covered by tangent points could also be reconstructed, but with quickly deteriorating quality. As in all tomographic reconstructions, measured structures are smeared along the ~~line-of-sights~~ lines-of-sight of the measurements if not constrained by measurements taken at different angles. Due to the curvature of the Earth, thick clouds measured at low altitudes are smeared along the line-

460 of-sight, which curves upwards from the tangent points and causes high extinction values at implausible altitudes — which is one of the reasons we employed the PV-dependent regularization scheme. Please note that due to the geometry of satellite measurements, the overlap of the ~~line-of-sights~~ lines-of-sight is much better, which prevents such ~~artefacts~~artifacts. The results of the reconstruction are depicted in Fig. 13. The two horizontal cross-sections show retrieved extinction values at two altitudes. At 10.5 km, one can see two cloud structures close to Iceland, a vertically thick and horizontally extended cloud at 20°W and

465 the thin cirrus cloud previously discussed at 16°W. The North-South extension already visible from Fig. 12 is also present here. Neither of the clouds visible at 10.5 km extends up to 12.5 km, where several small clouds close to the flight path are reproduced by the retrieval, which are associated to the vertically elongated areas of increased radiance in Fig. 12.

A theoretical analysis of the achieved resolution gives similar results to our previous work on deriving temperature structures (Krisch et al., 2018). Within the well-resolved volume the analysis shows an information content of about 0.05, i.e. 20 samples

470 share about one degree of freedom; outside it drops to an order of magnitude less, but numerical instabilities of the involved

15

equation systems make this difficult to compute precisely. Some systematic uncertainty due to uncertainty in the line-of-sight might bias the cloud tops estimate[2]. The vertical resolution in the area of the cirrus clouds is in the order of 300 m decreasing to 400 m for lower levels. The horizontal resolution is on the order of 30 km in the flight-track-direction and 70 km orthogonal to that. Circular flight patterns, or better, a backwards-viewing limb satellite could further improve the horizontal resolution (Ungermann et al., 2011; Krisch et al., 2017).

While the vertical extent, especially the cloud top, can be deduced with very high precision compared to nadir viewing instruments, it is not obvious that the horizontal extent was properly derived. For verification and comparison of quality of both, we used nadir viewing images of the Spinning Enhanced Visible and Infrared Imager (SEVIRI; Schmetz et al., 2002) on the second generation operational weather satellite Meteosat (MSG) and the Moderate Resolution Imaging Spectroradiometer (MODIS; Platnick et al., 2015, Platnick et al., 2017) on the Terra satellite. Due to its geostationary orbit, SEVIRI offers a good temporal coverage. Two spectral channels are shown in Fig. 14. The image from the visible spectrum at 0.8 μm shows scattered light from clouds at all altitudes. The second channel at 12.0 μm shows the brightness temperature of infrared light emitted by the ground and clouds (while scattering also plays a role here, we believe its influence to be small enough such that we can neglect it for this qualitative discussion). The 12 micron channel was selected as it uses the same spectral region that is also used in the GLORIA extinction retrieval. Clouds at higher altitude have a smaller brightness temperature than clouds at lower altitudes due to their lower temperature. Both images were taken at 12:00 UTC, which corresponds roughly to the mid-point of GLORIA measurements. In addition, we used the cloud top product from the MODIS instrument that passed over our measurement area in low Earth orbit around 13:08 UTC, which is only slightly beyond GLORIA's measurement period, and still reasonably close to compare the cloud top altitudes. However, the horizontal position might have been shifted due to advection and small clouds may also appear and disappear due to condensation and evaporation. Figure 15 shows the level 2 cloud top altitude product.

We focus first on region A in Figs. 13, 14, and 15. The GLORIA radiance and extinction data shows here an optically thick cloud within the jet-stream vertically ranging over several kilometers topping out at ≈11 km. This agrees with the MODIS cloud top data (mostly 10.5 km with some pixels slightly above 11.0 km) and is also consistent with the low brightness temperatures (<260 K) in the SEVIRI 12 micron band. In the horizontal, both, SEVIRI and MODIS see the high altitude cloud in the same position filling approximately the same area in region A and indicating no significant horizontal movement between both measurements. However, the GLORIA measurements fill a larger fraction of region A, which we attribute to the horizontal and temporal smearing of the retrieval (also here, a fast moving satellite would be subject to less temporal smearing due to a changing scene). The SEVIRI time series shows that the front is moving quickly eastwards and the 12:15 UTC image agrees already much better with our data (please note that the images containing most information were taken around 12:22 UTC pointing at 126° in relation to aircraft heading).

Second, we compare the structures found in region B in the same figures. There is a cloud stretching in a north-south direction for several 100 km with a brightness temperature of 272±1 K according to SEVIRI. The structure and location of the cloud

---

[2]current estimates of our pointing accuracy are in the order of 0.05–0.1°, which translates to a bias of 50 m 5 km below the aircraft, getting progressively worse towards lower altitudes.

visible in SEVIRI data compares ~~favourably~~ favorably with a cloud located at the same horizontal position at 10 to 10.75 km altitude in the GLORIA extinction retrieval (only one layer is depicted in Fig. 13). The magnitude of derived extinction indicates that the cloud is quite transparent in the nadir view such that the brightness temperature of SEVIRI is certainly largely caused by warmer air and haze of lower altitudes. This cloud ($\approx$ ~~1~~1.5 km thick with an extinction of $\approx$ ~~0.1~~0.014 ~~)~~ km^{-1}) and hence should reduce the measured nadir brightness temperature by $\approx$ ~~4~~1.3 K, which is roughly consistent with the difference of ~~3~~1.5 K observed by SEVIRI between the cloud and surrounding air. Please note that the cirrus cloud is well visible in the optical regime in Fig. 11. Also MODIS sees a quite similar cloud, but assigns it a cloud top altitude of below 1000 m consistent with the high brightness temperature visible in SEVIRI. For these thin layers of cirrus, a limb sounder provides much higher accuracy in cloud top determination than state-of-the-art cloud top products derived from nadir sounders (Weisz et al., 2007).

Third, region C is discussed. In contrast to the other, larger clouds, GLORIA detected very small clouds bringing it to its spatial detection limits as these clouds are small enough to fall into the gaps of the horizontal scans. However, the measurements indicate very thin cirrus clouds at an altitude of 12 to 13 km. The retrieval assembles the measurements to a region with small, spotty clouds of differing optical thickness with a top altitude of 12.75 km, which coincides with the cold point tropopause having here a temperature of $\approx$210 K. While SEVIRI and MODIS show similar small patchy clouds in region C, it is more difficult to assign the high altitude clouds retrieved from GLORIA. The cloud feature at the southern tip of region C agrees with a cloud feature measured by SEVIRI and MODIS. While the low brightness temperature of ~~SEVIRIs~~ SEVIRI's 12 μm channel indicates a high altitude cloud, as in region A, the MODIS cloud top altitude is below 2 km. From this discrepancy we deduce that these patchy clouds are probably too small and/or optically thin for IR nadir measurements to properly assign a cloud top altitude. While some of these have a comparably low brightness temperature of 265 K (the bright spot at the lowermost corner of region C), it is quite different from the 210 K corresponding to the altitude of the clouds detected by GLORIA. Due to the location close to the flight path, it could even be that the clouds that are visible in SEVIRI are unrelated clouds at lower altitudes as they would be outside the field-of-view of GLORIA. While the large cloud of region B was detected by MODIS albeit at a much too low altitude, these even thinner clouds have likely been missed totally. There are no high clouds in the MODIS data in region C and it is not easy to construct a relationship between the very small low clouds in region C in MODIS and our high clouds.

6 Conclusions

We presented a new cloud index product, the convex hull cloud index, which can exploit the higher measurement density of current and future over-sampling limb sounders. While it cannot improve upon the cloud identification for older limb-sounders such as MIPAS, it offers a significantly better cloud identification for higher measurement densities. We could show that it can properly locate clouds along the line-of-sight for many cases involving cirrus-clouds and thus reduce the number of false-positive cloud detection events by about 30 %. This method does not require a radiative transfer model and is computationally very cheap.

In addition, we introduced a tomographic extinction retrieval for cloud detection based on recent advances in retrieval techniques for limb sounders. The method uses the same algorithms and models used for 3-D temperature and trace gas reconstructions. In its current state, the required computational time is small compared to the measurement time thus allowing for real-time application. The tomographic extinction retrieval generated a statistically better result compared to the color ratio methods with a reduction of false positive detection events of more than 60 % compared to the standard cloud index. It excels in optically thin conditions, but could deal well with all typical cirrus clouds in the upper troposphere. For optically thick conditions given at lower altitudes the algorithms are naturally limited by the lack of information in the measurements by the limb sounders. Here, synergy with available nadir sounders could be exploited.

We finally applied the extinction retrieval to real measurements by the GLORIA limb sounder and could reconstruct several high and low altitude clouds in three dimensions. The vertical and horizontal position of these clouds was compared to images of the SEVIRI instrument and the cloud top altitude product based on MODIS data. We found good agreement in the general structure of the detected thick cirrus clouds. For thinner cirrus clouds, horizontal extent agreed, but vertical positioning disagreed. For very small and high cirrus clouds no strong correlation was found between the three products. Determining the cloud top altitude of the reconstructed clouds from GLORIA measurements is easily feasible with an accuracy of less than 300 m while the horizontal positioning is less certain. Due to the tomographic measurement principle a resolution of 30 to 70 km can be achieved, which may be further worsened depending on advection due to strong winds.

Summarising, we have shown that tomographic reconstruction schemes applied to densely sampled limb sounding observations allow to extract a wealth of information on high clouds, reaching beyond what standard methods can achieve. It demonstrates that these kind of observations are well suited to collect information on high clouds not being accessible by other kind of global measurements.

References

Beer, R.: Remote Sensing by Fourier Transform Spectrometry, Wiley-Interscience, 1992.

CALIPSO: https://eosweb.larc.nasa.gov/project/calipso/cal_lid_l2_05kmcpro-prov-v3-01_table, last access: 15 May, 2018.

Carlotti, M., Dinelli, B. M., Raspollini, P., and Ridolfi, M.: Geo-fit approach to the analysis of limb-scanning satellite measurements, Appl. Optics, 40, 1872–1885, https://doi.org/10.1364/AO.40.001872, 2001.

Castelli, E., Dinelli, B., Carlotti, M., Arnone, E., Papandrea, E., and Ridolfi, M.: Retrieving cloud geometrical extents from MIPAS/ENVISAT measurements with a 2-D tomographic approach, Opt. Express, 19, 20 704–20 721, https://doi.org/10.1364/OE.19.020704, 2011.

Christensen, O. M., Eriksson, P., Urban, J., Murtagh, D., Hultgren, K., and Gumbel, J.: Tomographic retrieval of water vapour and temperature around polar mesospheric clouds using Odin-SMR, Atmos. Meas. Tech., 8, 1981–1999, https://doi.org/10.5194/amt-8-1981-2015, 2015.

Dee, D. P., Uppala, S. M., Simmons, A. J., Berrisford, P., Poli, P., Kobayashi, S., Andrae, U., Balmaseda, M. A., Balsamo, G., Bauer, P., Bechtold, P., Beljaars, A. C. M., van de Berg, L., Bidlot, J., Bormann, N., Delsol, C., Dragani, R., Fuentes, M., Geer, A. J., Haimberger, L., Healy, S. B., Hersbach, H., Hòlm, E. V., Isaksen, L., Kållberg, P., Köhler, M., Matricardi, M., McNally, A. P., Monge-Sanz, B. M., Morcrette, J.-J., Park, B.-K., Peubey, C., de Rosnay, P., Tavolato, C., Thépaut, J.-N., and Vitart, F.: The ERA-Interim reanalysis: configuration and performance of the data assimilation system, Quart. J. Roy. Meteorol. Soc., 137, 553–597, https://doi.org/10.1002/qj.828, 2011.

Dudhia, A.: The Reference Forward Model (RFM), J. Quant. Spectrosc. Radiat. Transfer, 186, 243–253, https://doi.org/doi:10.1016/j.jqsrt.2016.06.018, 2017.

ESA: Report for Mission Selection: PREMIER, Tech. rep., European Space Agency, ESTEC, Keplerlaan 1, 2200 AG Noordwijk, The Netherlands, 2012.

Fischer, H., Birk, M., Blom, C., Carli, B., Carlotti, M., von Clarmann, T., Delbouille, L., Dudhia, A., Ehhalt, D., Endemann, M., Flaud, J. M., Gessner, R., Kleinert, A., Koopman, R., Langen, J., López-Puertas, M., Mosner, P., Nett, H., Oelhaf, H., Perron, G., Remedios, J., Ridolfi, M., Stiller, G., and Zander, R.: MIPAS: an instrument for atmospheric and climate research, Atmos. Chem. Phys., 8, 2151–2188, https://doi.org/10.5194/acp-8-2151-2008, 2008.

Friedl-Vallon, F., Gulde, T., Hase, F., Kleinert, A., Kulessa, T., Maucher, G., Neubert, T., Olschewski, F., Piesch, C., Preusse, P., Rongen, H., Sartorius, C., Schneider, H., Schönfeld, A., Tan, V., Bayer, N., Blank, J., Dapp, R., Ebersoldt, A., Fischer, H., Graf, F., Guggenmoser, T., Höpfner, M., Kaufmann, M., Kretschmer, E., Latzko, T., Nordmeyer, H., Oelhaf, H., Orphal, J., Riese, M., Schardt, G., Schillings, J., Sha, M. K., Sumińska-Ebersoldt, O., and Ungermann, J.: Instrument concept of the imaging Fourier transform spectrometer GLORIA, Atmos. Meas. Tech., 7, 3565–3577, https://doi.org/10.5194/amt-7-3565-2014, 2014.

Gayet, J.-F., Ovarlez, J., Shcherbakov, V., Ström, J., Schumann, U., Minikin, A., Auriol, F., Petzold, A., and Monier, M.: Cirrus cloud microphysical and optical properties at southern and northern midlatitudes during the INCA experiment, J. Geophys. Res. Atmos., 109, https://doi.org/10.1029/2004JD004803, 2004.

Gordley, L. L. and Russell, J. M.: Rapid inversion of limb radiance data using an emissivity growth approximation, Appl. Optics, 20, 807–813, https://doi.org/10.1364/AO.20.000807, 1981.

Griessbach, S., Hoffmann, L., Höpfner, M., Riese, M., and Spang, R.: Scattering in infrared radiative transfer: A comparison between the spectrally averaging model JURASSIC and the line-by-line model KOPRA, J. Quant. Spectrosc. Radiat. Transfer, 127, 102–118, https://doi.org/10.1016/j.jqsrt.2013.05.004, 2013.

Griessbach, S., Hoffmann, L., Spang, R., and Riese, M.: Volcanic ash detection with infrared limb sounding: MIPAS observations and radiative transfer simulations, Atmos. Meas. Tech., 7, 1487–1507, https://doi.org/10.5194/amt-7-1487-2014, 2014.

Griessbach, S., Hoffmann, L., Spang, R., von Hobe, M., Müller, R., and Riese, M.: Infrared limb emission measurements of aerosol in the troposphere and stratosphere, Atmos. Meas. Tech., 9, 4399–4423, https://doi.org/10.5194/amt-9-4399-2016, 2016.

Griessbach, S., Hoffmann, L., Spang, R., Achtert, P., von Hobe, M., Mateshvili, N., Müller, R., Riese, M., Rolf, C., Seifert, P., and Vernier, J.-P.: Aerosol and cloud top height information of Envisat MIPAS measurements, Atmos. Meas. Tech., 13, 1243–1271, https://doi.org/10.5194/amt-13-1243-2020, 2020a.

Griessbach, S. et al.: Aerosol and cloud detection capabilities of infrared limb emission measurements, Atmos. Meas. Tech., in preparation, 2020b.

Hase, F. and Höpfner, M.: Atmospheric ray path modeling for radiative transfer algorithms, Appl. Optics, 38, 3129–3133, https://doi.org/10.1364/AO.38.003129, 1999.

Heymsfield, A. J., Krämer, M., Luebke, A., Brown, P., Cziczo, D. J., Franklin, C., Lawson, P., Lohmann, U., McFarquhar, G., Ulanowski, Z., and Van Tricht, K.: Cirrus Clouds, Meteorological Monographs, 58, 2.1–2.26, https://doi.org/10.1175/AMSMONOGRAPHS-D-16-0010.1, 2017.

Hoffmann, L.: Schnelle Spurengasretrieval für das Satellitenexperiment Envisat MIPAS, Tech. Rep. JUEL-4207, Forschungszentrum Jülich, Jülich, Germany, ISSN 0944-2952, 2006.

Höpfner, M., Ungermann, J., Borrmann, S., Wagner, R., Spang, R., Riese, M., Stiller, G., Appel, O., Batenburg, A. M., Bucci, S., Cairo, F., Dragoneas, A., Friedl-Vallon, F., Hünig, A., Johansson, S., Krasauskas, L., Legras, B., Leisner, T., Mahnke, C., Möhler, O., Molleker, S., Müller, R., Neubert, T., Orphal, J., Preusse, P., Rex, M., Saathoff, H., Stroh, F., Weigel, R., and Wohltmann, I.: Ammonium nitrate particles formed in upper troposphere from ground ammonia sources during Asian monsoons, Nature Geosci., 12, 1752–0908, https://doi.org/10.1038/s41561-019-0385-8, 2019.

IPCC: Climate Change 2007: The Physical Science Basis. Contributions of Working Group I to the Fourth Assessment Report of the Intergovernmental Panel on Climate Change, Cambridge University Press, 2007.

Jülich Supercomputing Centre: JURECA: Modular supercomputer at Jülich Supercomputing Centre, Journal of large-scale research facilities, 4, https://doi.org/10.17815/jlsrf-4-121-1, http://dx.doi.org/10.17815/jlsrf-4-121-1, 2018.

Kalicinsky, C., Grooss, J. U., Guenther, G., Ungermann, J., Blank, J., Hoefer, S., Hoffmann, L., Knieling, P., Olschewski, F., Spang, R., Stroh, F., and Riese, M.: Observations of filamentary structures near the vortex edge in the Arctic winter lower stratosphere, Atmos. Chem. Phys., 13, 10 859–10 871, https://doi.org/10.5194/acp-13-10859-2013, 2013.

Kent, G. S., Winker, D. M., Vaughan, M. A., Wang, P.-H., and Skeens, K. M.: Simulation of Stratospheric Aerosol and Gas Experiment (SAGE) II cloud measurements using airborne lidar data, J. Geophys. Res. Atmos., 102, 21 795–21 807, https://doi.org/10.1029/97JD01390, 1997.

Kleinert, A., Friedl-Vallon, F., Guggenmoser, T., Höpfner, M., Neubert, T., Ribalda, R., Sha, M. K., Ungermann, J., Blank, J., Ebersoldt, A., Kretschmer, E., Latzko, T., Oelhaf, H., Olschewski, F., and Preusse, P.: Level 0 to 1 processing of the imaging Fourier transform spectrometer GLORIA: generation of radiometrically and spectrally calibrated spectra, Atmos. Meas. Tech., 7, 4167–4184, https://doi.org/10.5194/amt-7-4167-2014, 2014.

Konopka, P., Günther, G., Müller, R., dos Santos, F. H. S., Schiller, C., Ravegnani, F., Ulanovsky, A., Schlager, H., Volk, C. M., Viciani, S., Pan, L. L., McKenna, D.-S., and Riese, M.: Contribution of mixing to upward transport across the tropical tropopause layer (TTL), Atmos. Chem. Phys., 7, 3285–3308, https://doi.org/10.5194/acp-7-3285-2007, 2007.

Kox, S., Bugliaro, L., and Ostler, A.: Retrieval of cirrus cloud optical thickness and top altitude from geostationary remote sensing, Atmos. Meas. Tech., 7, 3233–3246, https://doi.org/10.5194/amt-7-3233-2014, 2014.

Krämer, M., Rolf, C., Spelten, N., Afchine, A., Fahey, D., Jensen, E., Khaykin, S., Kuhn, T., Lawson, P., Lykov, A., Pan, L. L., Riese, M.,
Rollins, A., Stroh, F., Thornberry, T., Wolf, V., Woods, S., Spichtinger, P., Quaas, J., and Sourdeval, O.: A Microphysics Guide to Cirrus –
Part II: Climatologies of Clouds and Humidity from Observations, Atmos. Chem. Phys. Discuss., 2020, 1–63, https://doi.org/10.5194/acp-
2020-40, https://www.atmos-chem-phys-discuss.net/acp-2020-40/, 2020.

Krisch, I., Preusse, P., Ungermann, J., Dörnbrack, A., Eckermann, S. D., Ern, M., Friedl-Vallon, F., Kaufmann, M., Oelhaf, H., Rapp, M.,
Strube, C., and Riese, M.: First tomographic observations of gravity waves by the infrared limb imager GLORIA, Atmos. Chem. Phys.,
17, 14 937–14 953, https://doi.org/10.5194/acp-17-14937-2017, 2017.

Krisch, I., Ungermann, J., Preusse, P., Kretschmer, E., and Riese, M.: Limited angle tomography of mesoscale gravity waves by the infrared
limb-sounder GLORIA, Atmos. Meas. Tech., 11, 4327–4344, https://doi.org/10.5194/amt-11-4327-2018, https://www.atmos-meas-tech.
net/11/4327/2018/, 2018.

Levenberg, K.: A method for the solution of certain nonlinear problems in least squares, Quart. Appl. Math., 2, 164–168, 1944.

Livesey, N., Van Snyder, W., Read, W., and Wagner, P.: Retrieval algorithms for the EOS Microwave limb sounder (MLS), IEEE T. Geosci.
Remote. Sens., 44, 1144 – 1155, https://doi.org/10.1109/TGRS.2006.872327, 2006.

Livesey, N. J. and Read, W. G.: Direct Retrieval of Line-of-Sight Atmospheric Structure from Limb Sounding Observations, Geophys. Res.
Lett., 27, 891–894, 2000.

Luebke, A. E., Afchine, A., Costa, A., Grooß, J.-U., Meyer, J., Rolf, C., Spelten, N., Avallone, L. M., Baumgardner, D., and Krämer, M.:
The origin of midlatitude ice clouds and the resulting influence on their microphysical properties, Atmos. Chem. Phys., 16, 5793–5809,
https://doi.org/10.5194/acp-16-5793-2016, 2016.

McKenna, D. S., Konopka, P., Grooß, J.-U., Günther, G., Müller, R., Spang, R., Offermann, D., and Orsolini, Y.: A new
Chemical Lagrangian Model of the Stratosphere (CLaMS) 1. Formulation of advection and mixing, J. Geophys. Res., 107,
https://doi.org/10.1029/2000JD000114, 2002.

Mejia, F. A., Kurtz, B., Levis, A., Íñigo de la Parra, and Kleissl, J.: Cloud tomography applied to sky images: A virtual testbed, Solar Energy,
176, 287 – 300, https://doi.org/https://doi.org/10.1016/j.solener.2018.10.023, 2018.

Nazaryan, H., McCormick, M. P., and Menzel, W. P.: Global characterization of cirrus clouds using CALIPSO data, J. Geophys. Res. Atmos.,
113, https://doi.org/10.1029/2007JD009481, 2008.

Norton, R. H. and Beer, R.: New apodizing functions for Fourier spectrometry, J. Opt. Soc. Am., 66, 259–264, see errata, 1976.

Platnick, S., Ackerman, S., King, M., and et al.: MODIS Atmosphere L2 Cloud Product (06_L2), NASA MODIS Adaptive Processing
System, Goddard Space Flight Center, USA, https://doi.org/10.5067/MODIS/MOD06_L2.061, 2015.

Platnick, S., Meyer, K. G., King, M. D., Wind, G., Amarasinghe, N., Marchant, B., Arnold, G. T., Zhang, Z., Hubanks, P. A., Holz, R. E.,
Yang, P., Ridgway, W. L., and Riedi, J.: The MODIS Cloud Optical and Microphysical Products: Collection 6 Updates and Examples
From Terra and Aqua, IEEE T. Geosci. Remote. Sens., 55, 502–525, 2017.

Ploeger, F., Konopka, P., Günther, G., Grooß, J.-U., and Müller, R.: Impact of the vertical velocity scheme on modeling transport in the
tropical tropopause layer, J. Geophys. Res. Atmos., 115, D03 301, https://doi.org/10.1029/2009JD012023, 2010.

Remedios, J. J., Leigh, R. J., Waterfall, A. M., Moore, D. P., Sembhi, H., Parkes, I., Greenough, J., Chipperfield, M., and Hauglustaine, D.:
MIPAS reference atmospheres and comparisons to V4.61/V4.62 MIPAS level 2 geophysical data sets, Atmos. Chem. Phys. Discuss., 7,
9973–10 017, https://doi.org/10.5194/acpd-7-9973-2007, 2007.

Riese, M., Oelhaf, H., Preusse, P., Blank, J., Ern, M., Friedl-Vallon, F., Fischer, H., Guggenmoser, T., Höpfner, M., Hoor, P., Kaufmann,
M., Orphal, J., Plöger, F., Spang, R., Suminska-Ebersoldt, O., Ungermann, J., Vogel, B., and Woiwode, W.: Gimballed Limb Observer for

Radiance Imaging of the Atmosphere (GLORIA) scientific objectives, Atmos. Meas. Tech., 7, 1915–1928, https://doi.org/10.5194/amt-7-1915-2014, 2014.

Schmetz, J., Pili, P., Tjemkes, S., Just, D., Kerkmann, J., Rota, S., and Ratier, A.: AN INTRODUCTION TO METEOSAT SECOND GENERATION (MSG), Bulletin of the American Meteorological Society, 83, 977–992, https://doi.org/10.1175/1520-0477(2002)083<0977:AITMSG>2.3.CO;2, 2002.

Sembhi, H., Remedios, J., Trent, T., Moore, D. P., Spang, R., Massie, S., and Vernier, J.-P.: MIPAS detection of cloud and aerosol particle occurrence in the UTLS with comparison to HIRDLS and CALIOP, Atmos. Meas. Tech., 5, 2537–2553, https://doi.org/10.5194/amt-5-2537-2012, 2012.

Spang, R., Riese, M., Eidmann, G., Offermann, D., and Wang, P. H.: A Detection Method for Cirrus Clouds Using CRISTA 1 and 2 Measurements, Adv. Space Res., 27, 1629–1634, 2001a.

Spang, R., Riese, M., and Offermann, D.: CRISTA-2 observations of the south polar vortex in winter 1997: A new dataset for polar process studies, Geophys. Res. Lett., 28, 3159–3162, 2001b.

Spang, R., Hoffmann, L., Kullmann, A., Olschewski, F., Preusse, P., Knieling, P., Schroeder, S., Stroh, F., Weigel, K., and Riese, M.: High resolution limb observations of clouds by the CRISTA-NF experiment during the SCOUT-O3 tropical aircraft campaign, Adv. Space Res., 42, 1765–1775, https://doi.org/10.1016/j.asr.2007.09.036, 2008.

Spang, R., Arndt, K., Dudhia, A., Höpfner, M., Hoffmann, L., Hurley, J., Grainger, R. G., Griessbach, S., Poulsen, C., Remedios, J. J., Riese, M., Sembhi, H., Siddans, R., Waterfall, A., and Zehner, C.: Fast cloud parameter retrievals of MIPAS/Envisat, Atmos. Chem. Phys., 12, 7135–7164, https://doi.org/10.5194/acp-12-7135-2012, 2012.

Spang, R., Günther, G., Riese, M., Hoffmann, L., Müller, R., and Griessbach, S.: Satellite observations of cirrus clouds in the Northern Hemisphere lowermost stratosphere, Atmos. Chem. Phys., 15, 927–950, https://doi.org/10.5194/acp-15-927-2015, 2015.

Spichtinger, P. and Gierens, K. M.: Modelling of cirrus clouds — Part 1a: Model description and validation, Atmos. Chem. Phys., 9, 685–706, https://doi.org/10.5194/acp-9-685-2009, 2009.

Steck, T., Höpfner, M., von Clarmann, T., and Grabowski, U.: Tomographic retrieval of atmospheric parameters from infrared limb emission observations, Appl. Optics, 44, 3291–3301, https://doi.org/10.1364/AO.44.003291, 2005.

Tikhonov, A. N. and Arsenin, V. Y.: Solutions of ill-posed problems, Winston, Washington D.C., USA, 1977.

Ungermann, J., Hoffmann, L., Preusse, P., Kaufmann, M., and Riese, M.: Tomographic retrieval approach for mesoscale gravity wave observations by the PREMIER Infrared Limb-Sounder, Atmos. Meas. Tech., 3, 339–354, https://doi.org/10.5194/amt-3-339-2010, 2010.

Ungermann, J., Blank, J., Lotz, J., Leppkes, K., Hoffmann, L., Guggenmoser, T., Kaufmann, M., Preusse, P., Naumann, U., and Riese, M.: A 3-D tomographic retrieval approach with advection compensation for the air-borne limb-imager GLORIA, Atmos. Meas. Tech., 4, 2509–2529, https://doi.org/10.5194/amt-4-2509-2011, http://www.atmos-meas-tech.net/4/2509/2011/, 2011.

Ungermann, J., Blank, J., Dick, M., Ebersoldt, A., Friedl-Vallon, F., Giez, A., Guggenmoser, T., Höpfner, M., Jurkat, T., Kaufmann, M., Kaufmann, S., Kleinert, A., Krämer, M., Latzko, T., Oelhaf, H., Olchewski, F., Preusse, P., Rolf, C., Schillings, J., Suminska-Ebersoldt, O., Tan, V., Thomas, N., Voigt, C., Zahn, A., Zöger, M., and Riese, M.: Level 2 processing for the imaging Fourier transform spectrometer GLORIA: derivation and validation of temperature and trace gas volume mixing ratios from calibrated dynamics mode spectra, Atmos. Meas. Tech., 8, 2473–2489, https://doi.org/10.5194/amt-8-2473-2015, 2015.

von Clarmann, T., Glatthor, N., Grabowski, U., Höpfner, M., Kellmann, S., Kiefer, M., Linden, A., Tsidu, G. M., Milz, M., Steck, T., Stiller, G. P., Wang, D. Y., and Fischer, H.: Retrieval of temperature and tangent altitude pointing from limb emission spec-

tra recorded from space by the Michelson Interferometer for Passive Atmospheric Sounding (MIPAS), J. Geophys. Res., 108, https://doi.org/10.1029/2003JD003602, 2003.

von Clarmann, T., De Clercq, C., Ridolfi, M., Höpfner, M., and Lambert, J.-C.: The horizontal resolution of MIPAS, Atmos. Meas. Tech., 2, 47–54, https://doi.org/10.5194/amt-2-47-2009, 2009.

Weinreb, M. P. and Neuendorffer, A. C.: Method to Apply Homogeneous-path Transmittance Models to Inhomogeneous Atmospheres, J. Atmos. Sci., 30, 662–666, https://doi.org/10.1175/1520-0469(1973)030<0662:MTAHPT>2.0.CO;2, 1973.

Weisz, E., Li, J., Menzel, W. P., Heidinger, A. K., Kahn, B. H., and Liu, C.-Y.: Comparison of AIRS, MODIS, CloudSat and CALIPSO cloud top height retrievals, Geophys. Res. Lett., 34, https://doi.org/10.1029/2007GL030676, 2007.

Winker, D. M., Hunt, W. H., and McGill, M. J.: Initial performance assessment of CALIOP, Geophys. Res. Lett., 34, https://doi.org/10.1029/2007GL030135, 2007.

Winker, D. M., Vaughan, M. A., Omar, A., Hu, Y., Powell, K. A., Liu, Z., Hunt, W. H., and Young, S. A.: Overview of the CALIPSO Mission and CALIOP Data Processing Algorithms, Journal of Atmospheric and Oceanic Technology, 26, 2310–2323, https://doi.org/10.1175/2009JTECHA1281.1, 2009.

Cloud top altitude comparison			
Testcase	CI error	convex hull CI err.	ext. ret. error
CALIOP extinctions	1.08±2.29 km	0.71±2.03 km	0.47±1.50 km
10^{-1} CALIOP extinctions	0.66±2.14 km	0.16±1.96 km	0.16±1.32 km

Table 1. This table aggregates the difference between true cloud top altitude and determined cloud top altitude for 440 CALIOP orbits acquired in December 2012 for simulated IRLS measurements.

Cloud top shape comparison									
	CI			convex hull CI			ext. ret.		
Testcase	ok	fn	fp	ok	fn	fp	ok	fn	fp
CALIOP extinctions	74	1	24	80	4	16	89	4	7
10^{-1} CALIOP ext.	78	4	18	81	8	12	89	6	5

Table 2. This table aggregates the difference between true cloud top shape and determined cloud top shape for 440 CALIOP orbits acquired in December 2012 for simulated IRLS measurements. All values in percent. 'ok' means correctly detected, 'fn' is a false negative, 'fp' a false positive.
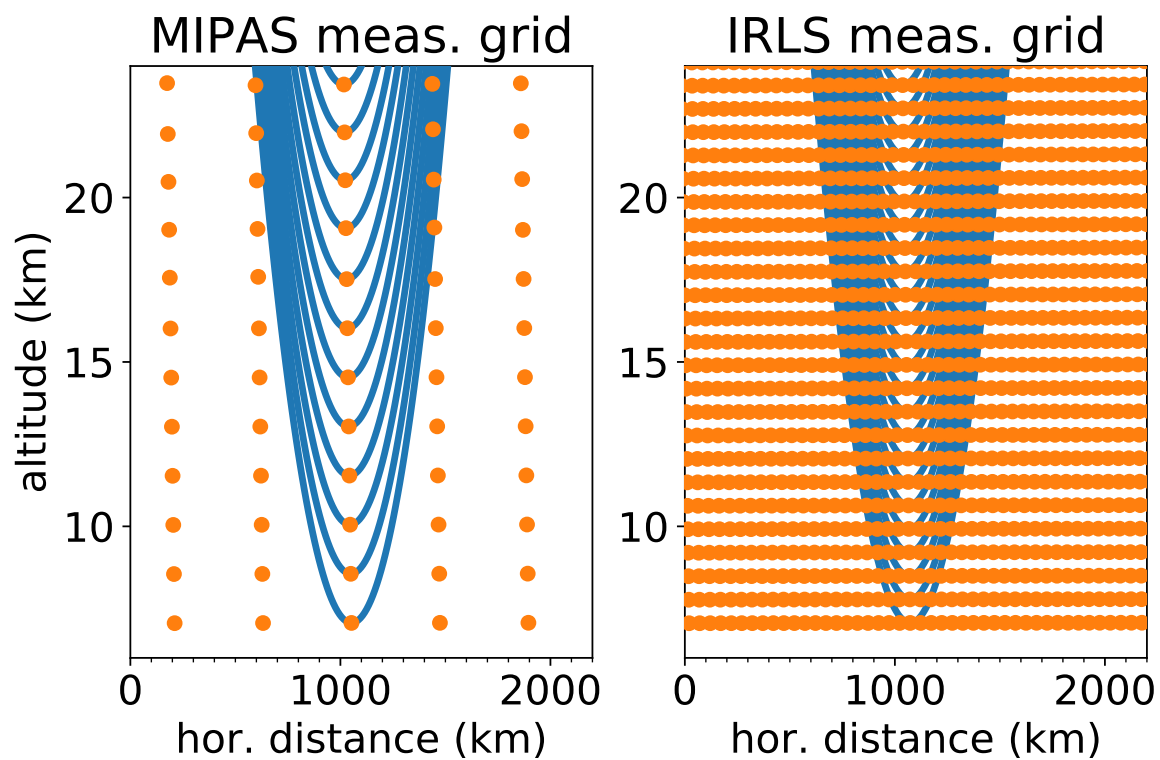
Figure 1. The measurement grid of a MIPAS-like instrument (left panel) and the IRLS (right panel). The blue lines indicate the ~~line-of-sights~~ lines-of-sight of ~~a~~ single ~~profile~~limb-scans. The orange dots indicate the tangent points of multiple adjacent profiles 2100 km along-track.
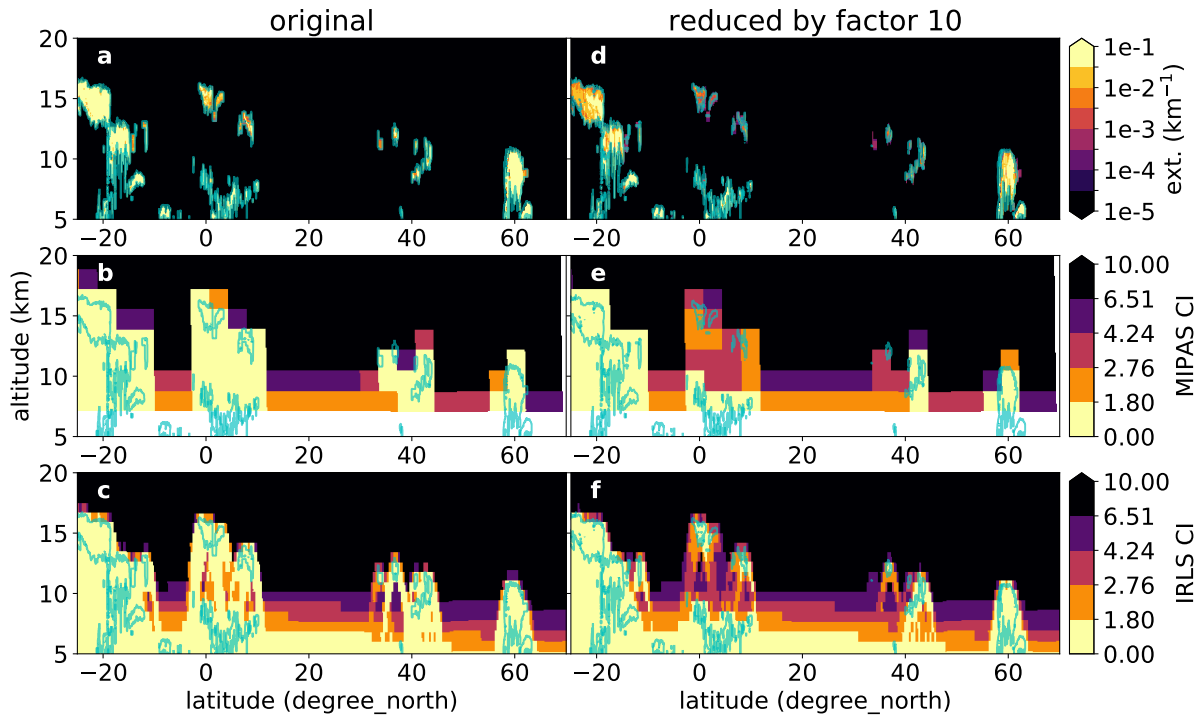
Figure 2. CALIOP extinction **(a)** and CALIOP extinction reduced by a factor of ten **(d)** (measured on 2009-12-01 from 03:37:36 UTC onward) as well as the associated CI derived from simulated MIPAS measurements in Panels **(b)** and **(e)**. The CI derived from simulated IRLS measurements is given in Panels **(c)** and **(f)**, respectively. The contour line for an extinction value of $10^{-3}\,\mathrm{km}^{-1}$ is shown as a light blue line in all panels. The satellite looks northwards in these simulations.
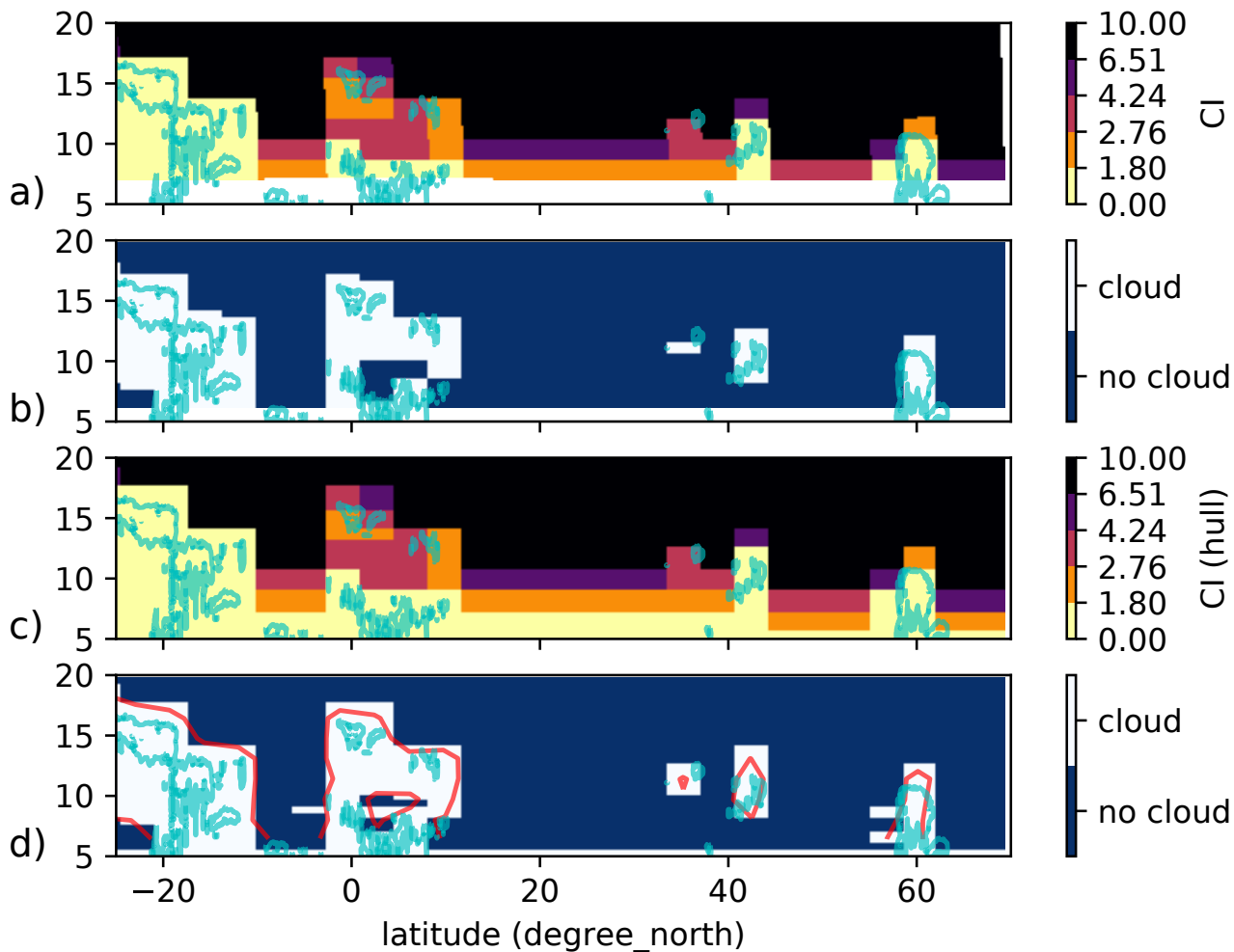
Figure 3. Result of the convex hull CI algorithm for MIPAS simulations based on CALIOP extinctions reduced by a factor of ten. The top panel **(a)** shows the CI at the location of tangent points. Panel **(b)** shows the location of clouds according to the altitude dependent CI threshold. Panel **(c)** shows the CI determined with the convex hull CI algorithm. Panel **(d)** shows the location of clouds according to the altitude dependent CI threshold. The cloud position from Panel (b) is shown as a red contour line for reference. The contour line for a 'true' extinction value of $10^{-3}\,\mathrm{km}^{-1}$ is shown as a light blue line in all panels. The satellite looks northwards in these simulations.
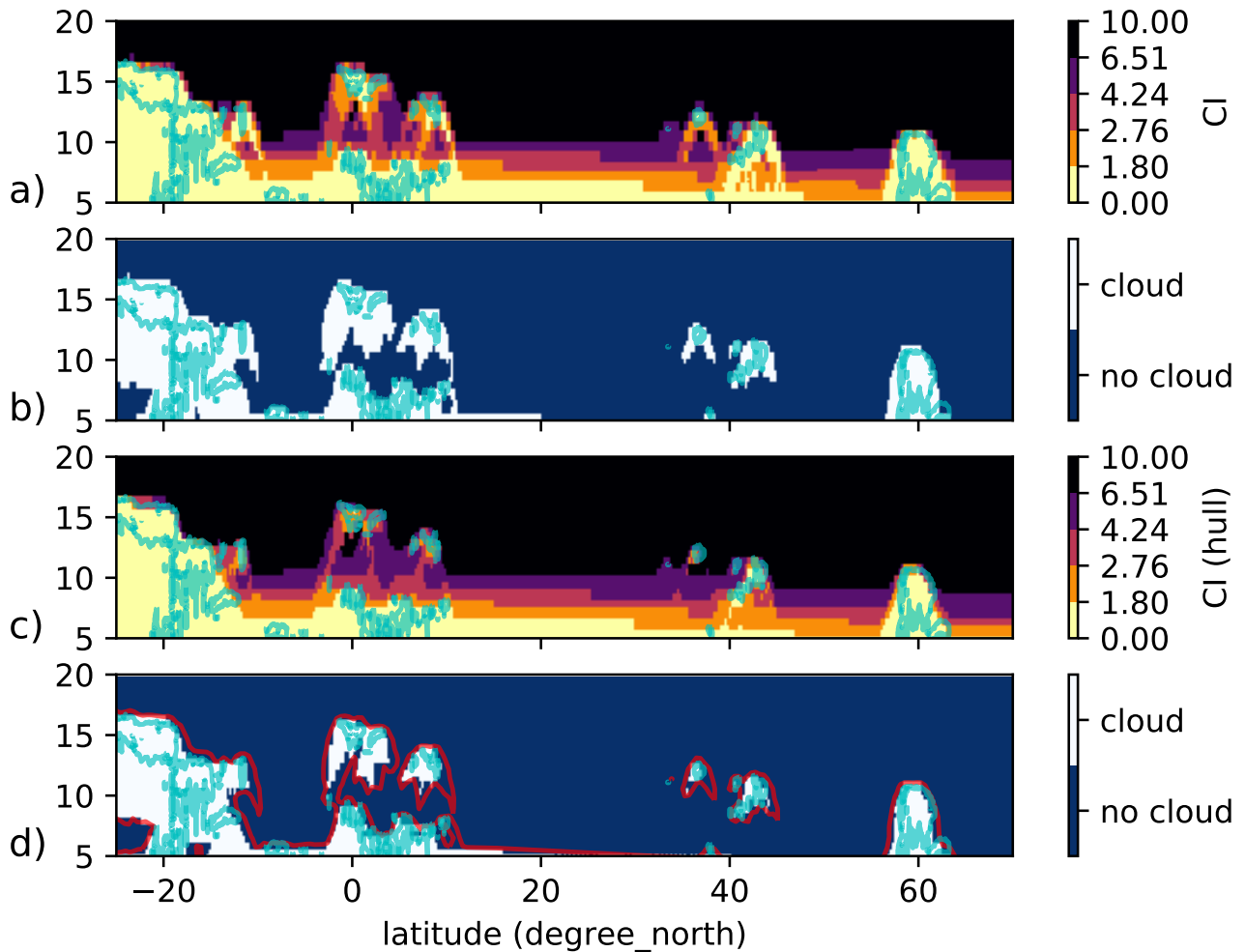
Figure 4. Result of the convex hull CI algorithm for IRLS simulations based on CALIOP extinctions reduced by a factor of ten. The top panel **(a)** shows the CI at the location of the tangent points. Panel **(b)** shows the location of clouds according to the altitude dependent CI threshold. Panel **(c)** shows the CI determined with the convex hull CI algorithm. Panel **(d)** shows the location of clouds according to the altitude dependent CI threshold. The cloud position from Panel (b) is shown as a red contour line for reference. The contour line for a 'true' extinction value of $10^{-3}\,\mathrm{km}^{-1}$ is shown as a light blue line in all panels. The satellite looks northwards in these simulations.
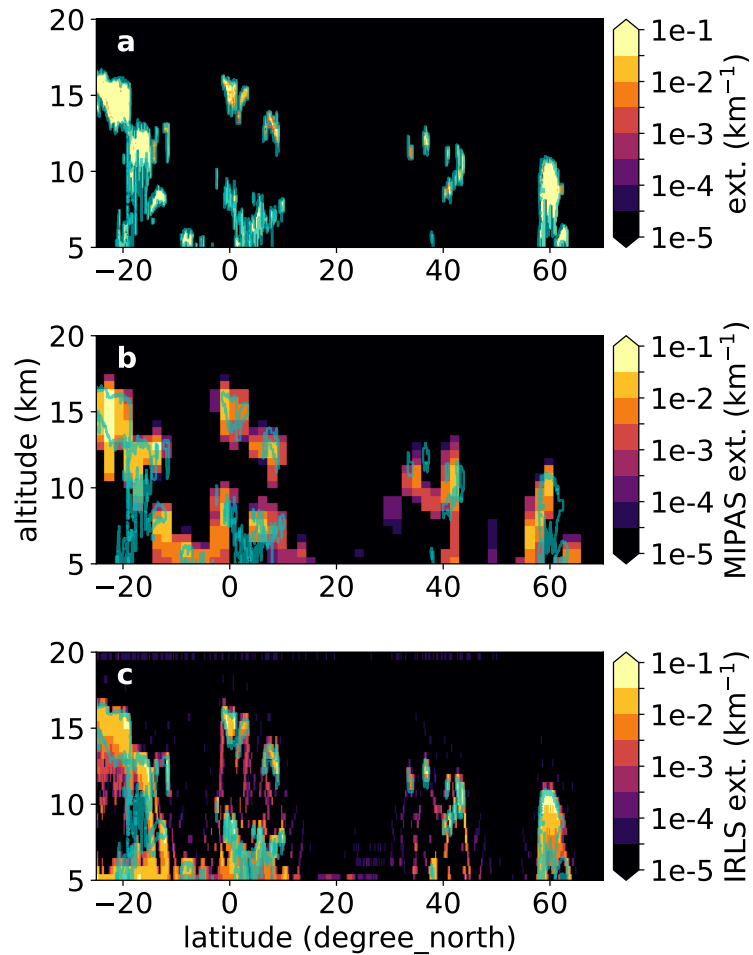
Figure 5. Retrieval of extinction from simulated measurements using CALIOP extinctions reduced by a factor of ten. Panel (**a**) shows the true extinction while Panel (**b**) shows the retrieved values for a MIPAS like instrument. Panel (**c**) gives the results for an instrument with higher measurement density such as the IRLS. The contour line for a 'true' extinction value of 10^{-3} km^{-1} is shown as a light blue line in all panels. The satellite looks northwards in these simulations.
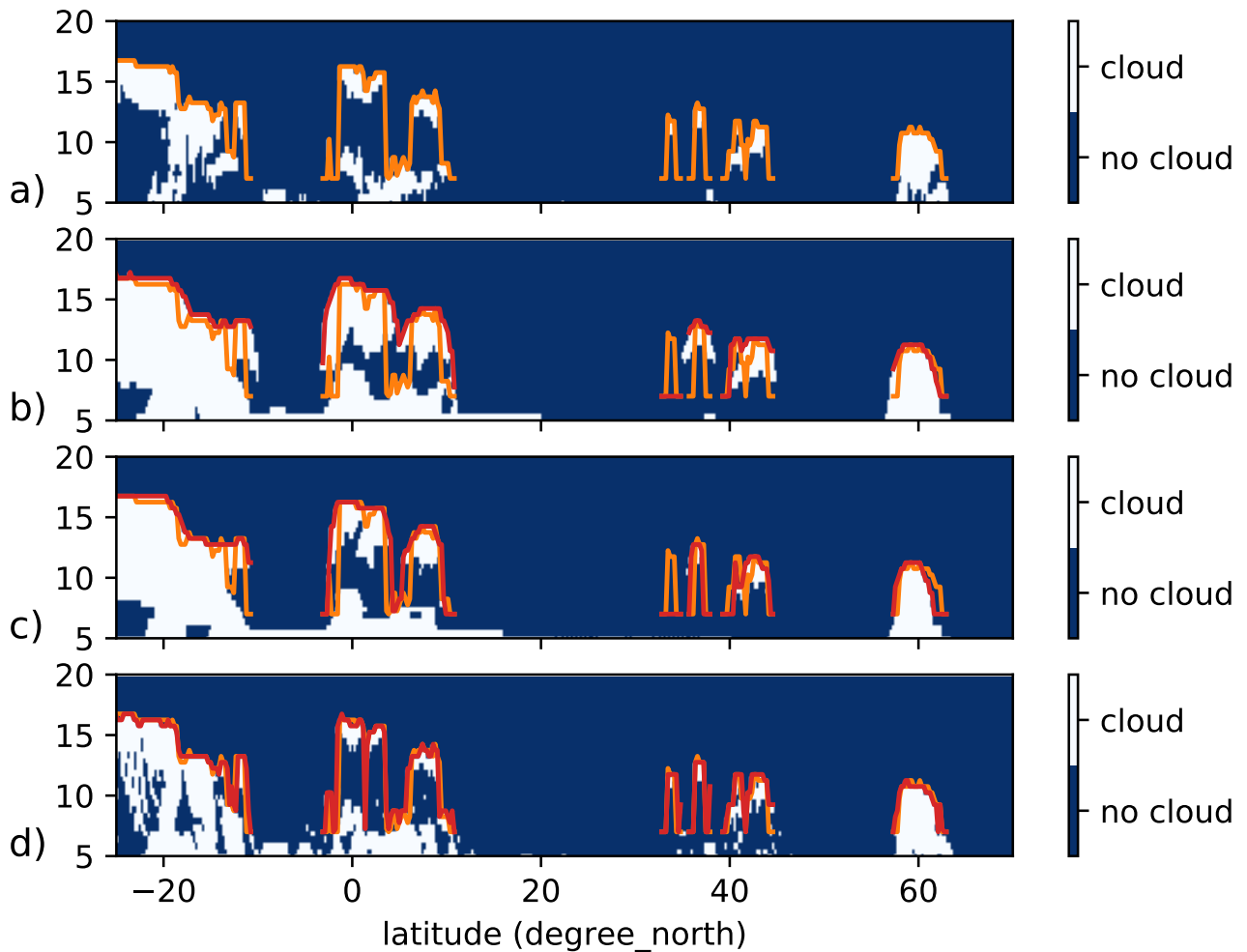
Figure 6. Comparison of cloud top detection capability for the various discussed methods and the IRLS instrument. Panel (**a**) shows the cloud extent contained in the CALIOP data. Panel (**b**) shows the cloud extent according to the CI. Panel (**c**) shows the cloud extent according to the convex hull CI algorithm. Panel (**d**) shows the cloud extent according to the tomographic extinction retrieval. In all panels, the orange line shows the true cloud top altitude, where clouds are present above 7 km with a lower limit of 7 km. The red line shows the cloud top altitude according to the depicted algorithm. The satellite looks northwards in these simulations.
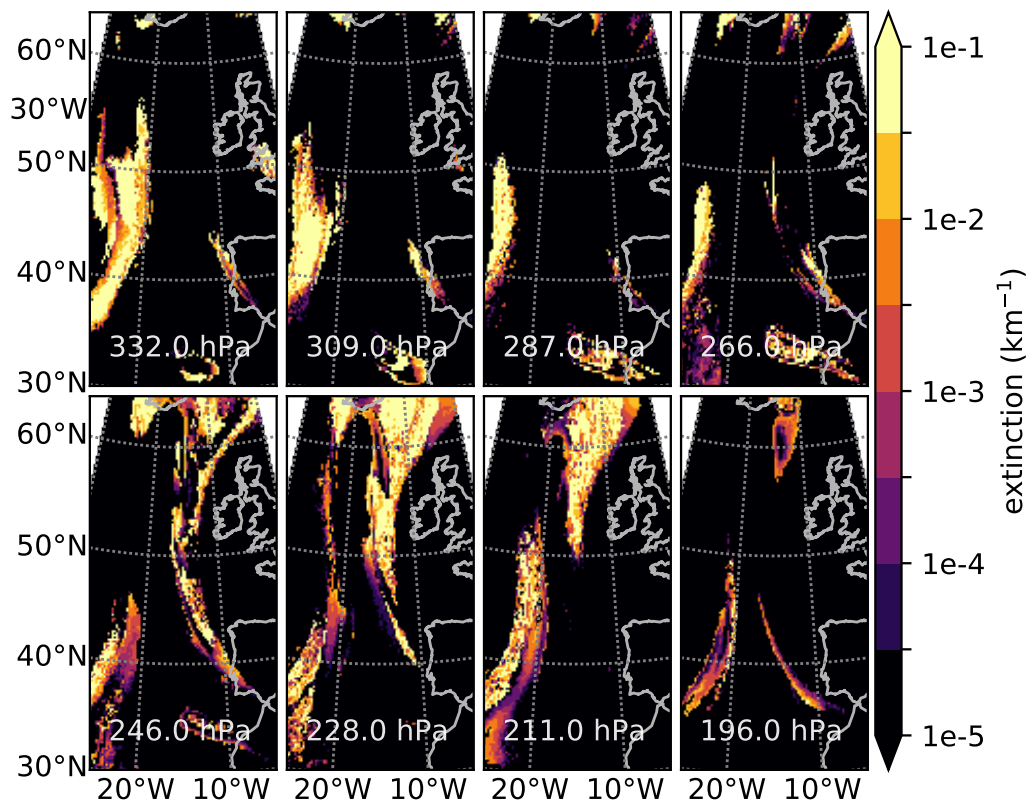
Figure 7. Extinction of a cirrus cloud simulated by CLaMS-ICE and computed from ice water content and particle radii.
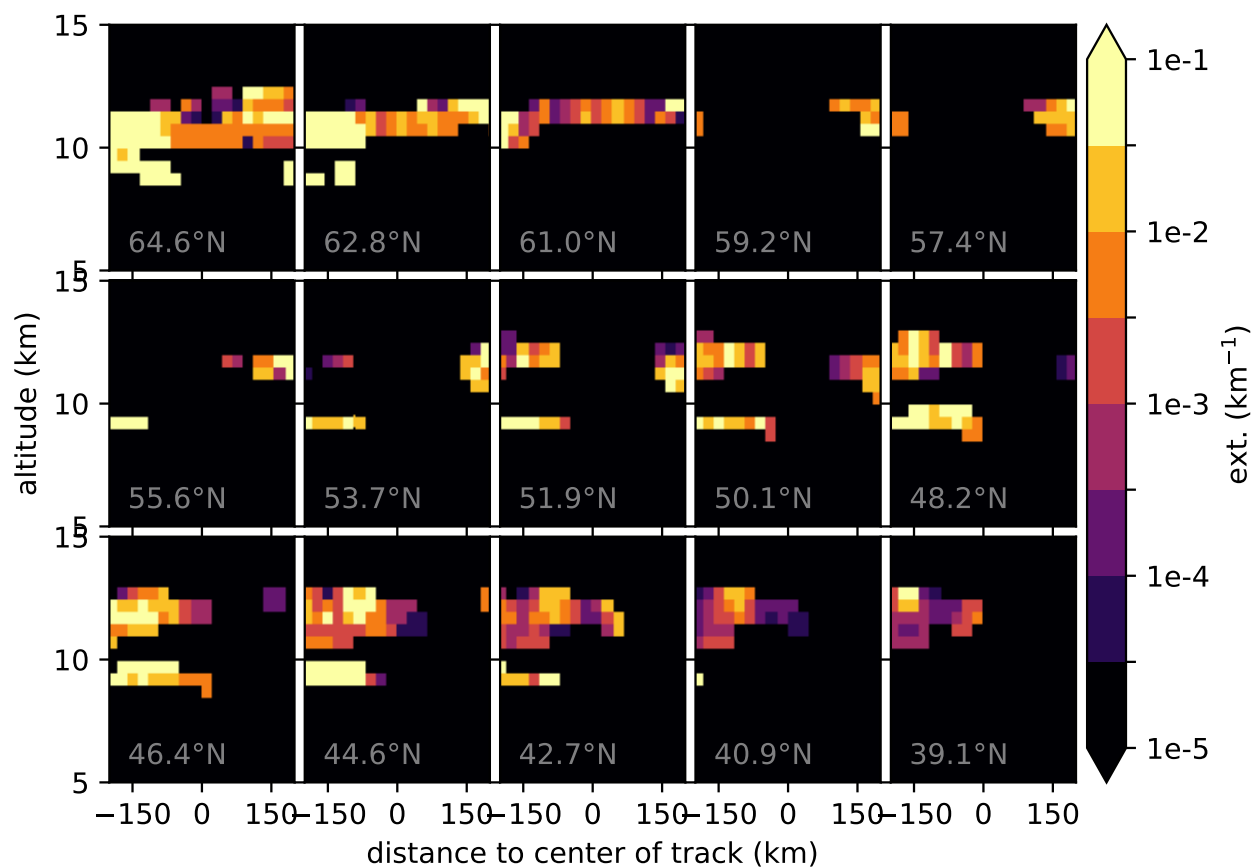
Figure 8. Cross-section through CLaMS-ICE extinction data corresponding roughly to the field-of-view of the IRLS. Only every second image of the IRLS is depicted.
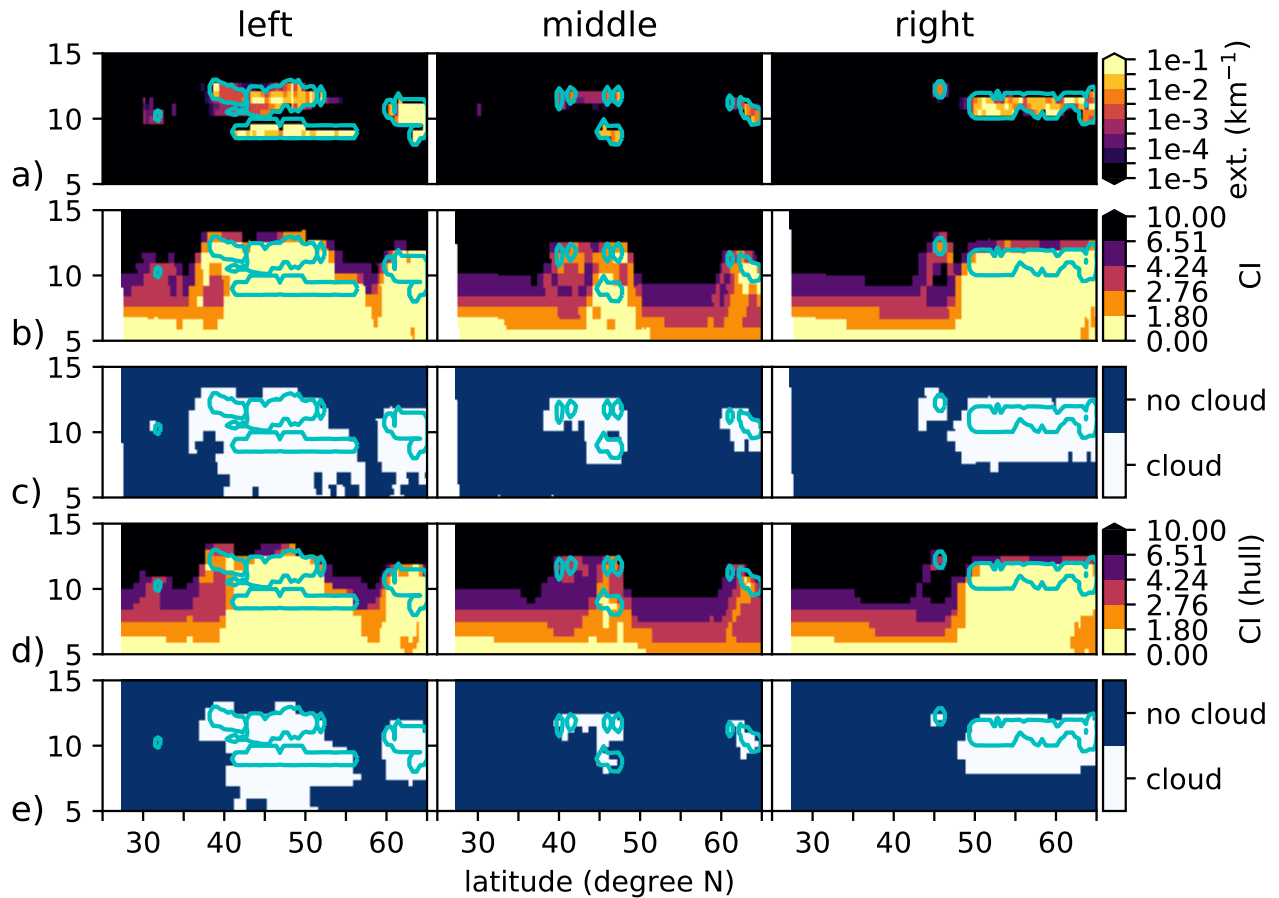
Figure 9. Cloud index and convex hull CI for three measurement tracks of a simulate IRLS instrument (left-most, center, and right-most). Panel **(a)** shows the ~~extinction values used for generating the simulated measurements. Panel **(b)** shows the~~ cloud index, Panel ~~**(b)**~~ **(c)** shows the corresponding cloud detection. Panel ~~**(c)**~~ **(d)** shows the CI as derived from the convex hull CI algorithm, whereas Panel ~~**(d)**~~ **(e)** shows the cloud detection for the convex hull CI. ~~Panel **(e)** shows the extinction values used for generating the simulated measurements.~~ The contour line for a 'true' extinction value of $10^{-3}\,\mathrm{km}^{-1}$ is shown as a light blue line in all panels.
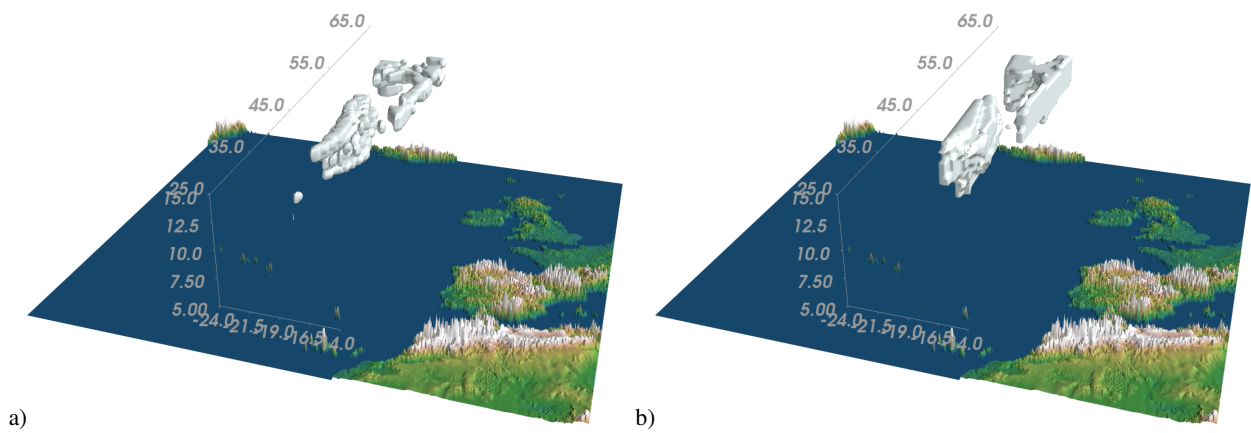
Figure 10. The true (panel (**a**)) and derived (panel (**b**)) cloud structure using the convex hull CI algorithm. Shown is a white contour surface for $10^{-3}\,\text{km}^{-1}$ in the measurement track of the IRLS. The vertical dimension is stretched by a factor of roughly 100. Due to the employed cylindrical projection, the measurements expand towards the back.
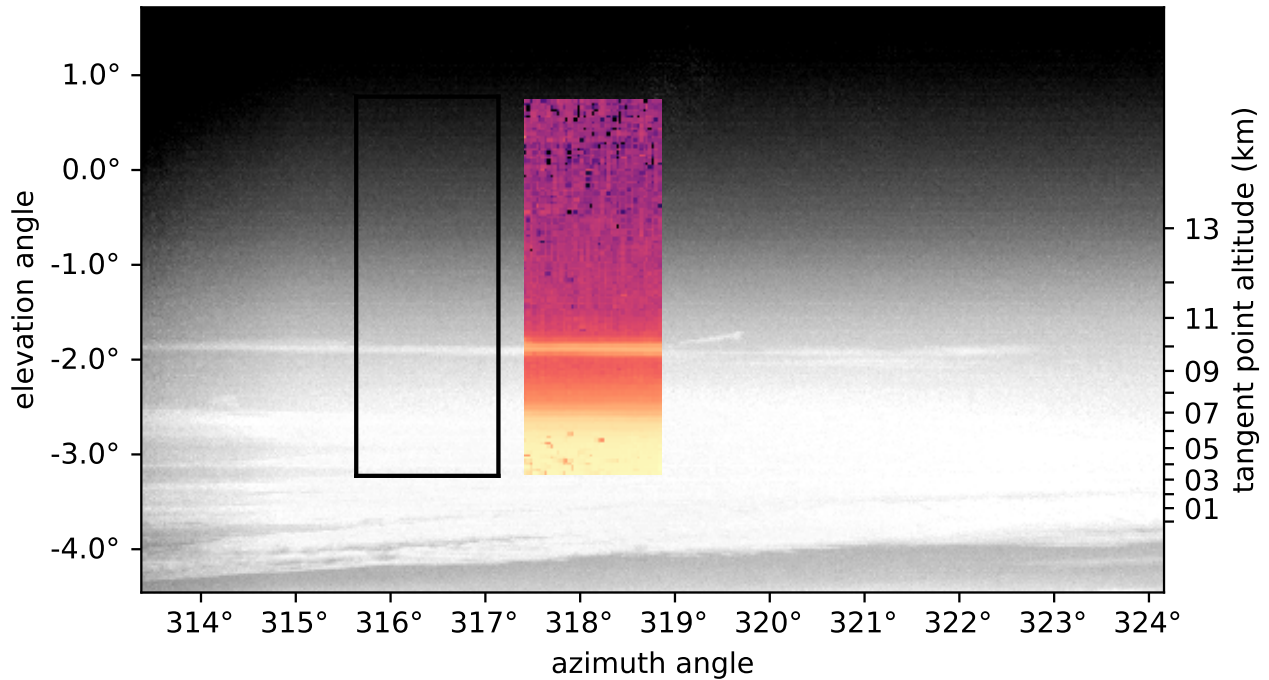
Figure 11. A superposition of a ~~visual~~ visible and infrared image taken at 11:50:31 UTC showing a cirrus cloud located at $10.5\,\text{km}$. The ~~visual~~ visible image ~~is similar to a normal camera and~~ has a much wider field-of-view than the infrared one. The infrared image has been extracted from the spectrally resolved GLORIA measurements and shows the averaged radiance over the spectral range from $831.2\,\text{cm}^{-1}$ to $835.0\,\text{cm}^{-1}$; it has also been shifted to the right for better comparability and the radiance is depicted in a logarithmic scale with arbitrary units; the black frame marks the original position. The altitude axis on the right gives an approximate tangent point altitude.
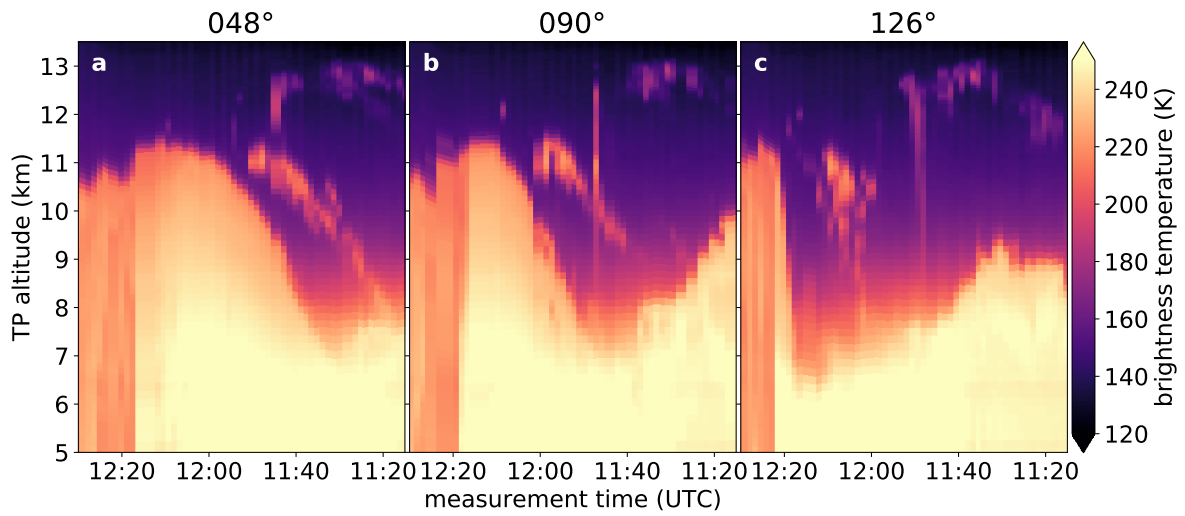
Figure 12. Brightness temperature of GLORIA measurements averaged over the wavenumber range from $831.2\,\mathrm{cm}^{-1}$ to $835\,\mathrm{cm}^{-1}$ (the same that is used as in the tomographic retrieval) over time sorted according to azimuth angle in relation to aircraft heading.
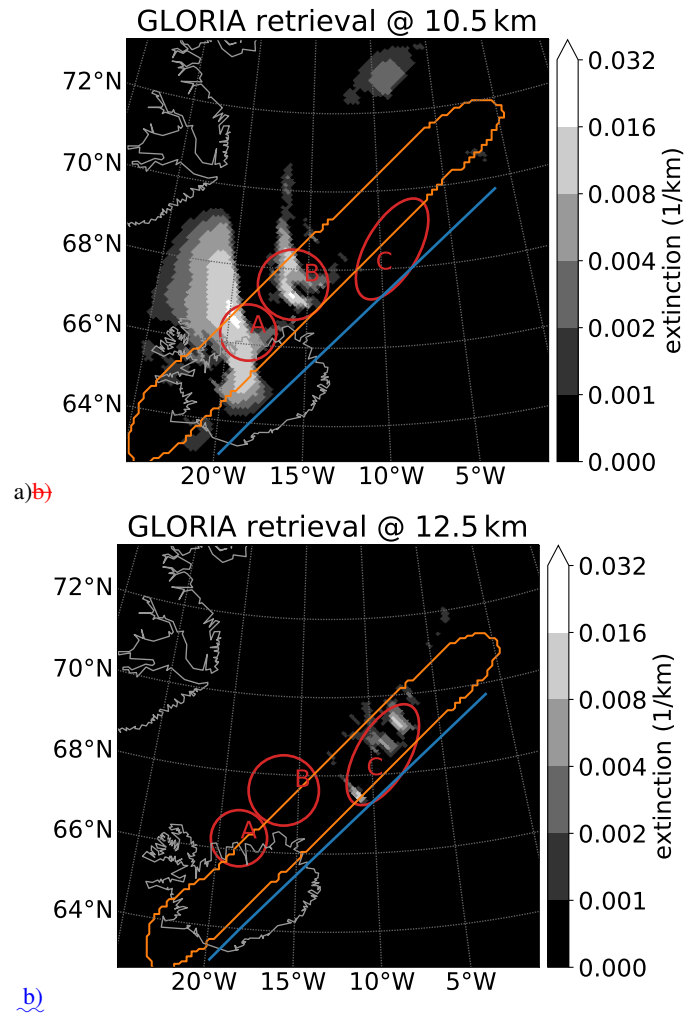
a)b)

b)

Figure 13. Cross-sections of extinction retrieved from GLORIA measurements. Panel **(a)** shows a horizontal cross-section at 10.5 km and panel **(b)** one at 12.5 km. Flight path is shown in blue, the trust region with high confidence in retrieval results around the tangent points of measurements is marked in orange. The three red ellipses mark areas of interest.
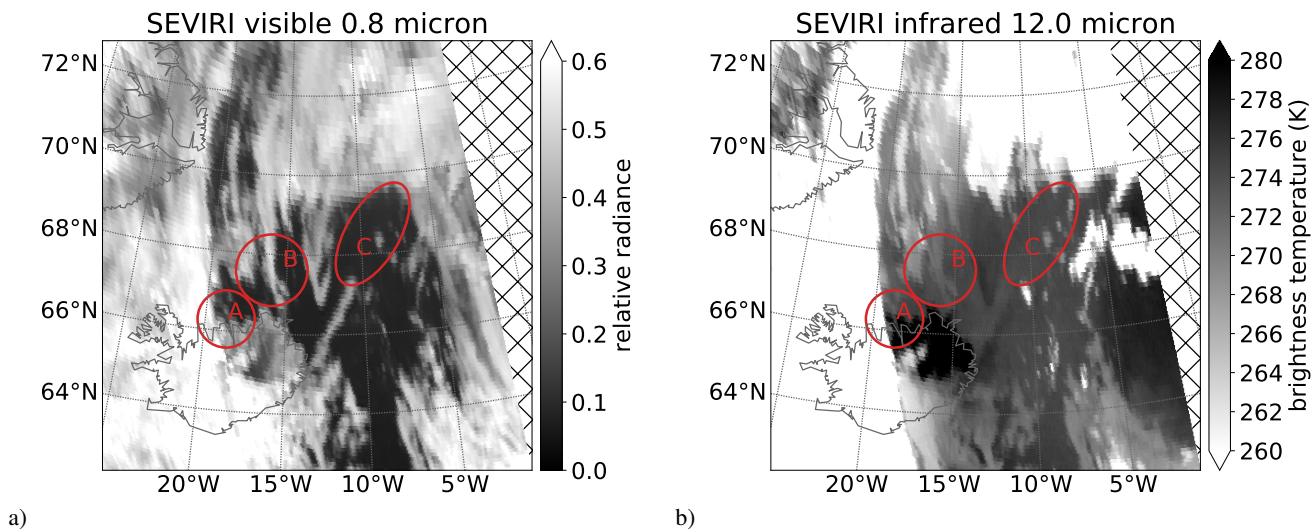
Figure 14. Two images taken by SEVIRI on Meteosat on 18th September 2017 at 12:00 UTC. Panel **(a)** shows the 0.8 micron visible channel in a relative scale and panel **(b)** shows the 12.0 micron infrared channel as brightness temperature. The three red ellipses mark areas of interest. Hatched areas indicate missing data.
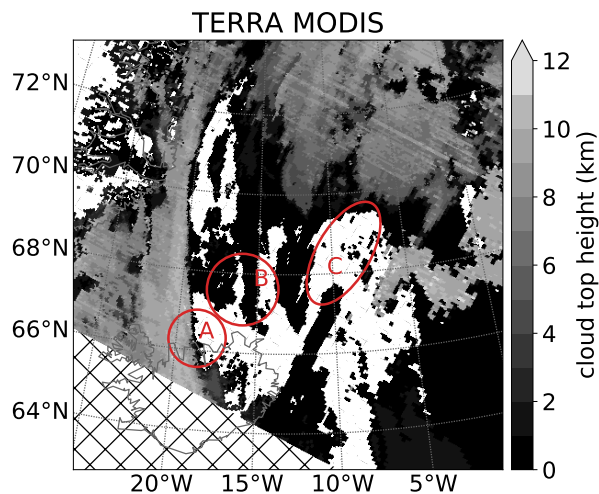

Figure 15. The cloud top altitude L2 product of MODIS on TERRA taken on 18th September 2017 around 13:08 UTC. White indicates no recognized cloud. The three red ellipses mark areas of interest. Hatched areas indicate missing data.